

RESEARCH ARTICLE



Rational design, synthesis, and molecular modelling insights of dual DNA binders/DHFR inhibitors bearing arylidene-hydrazinyl-1,3-thiazole scaffold with apoptotic and anti-migratory potential in breast MCF-7 cancer cells

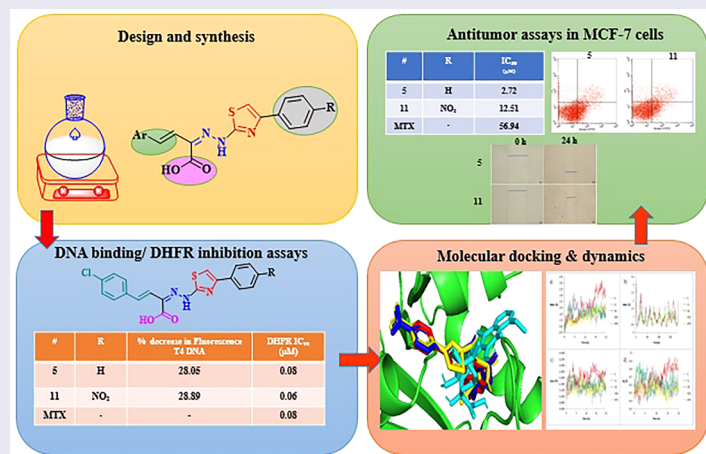
Marwa H. El-Wakil^a, Rasha A. Ghazala^b, Hadeel A. El-Dershaby^a, Danuta Drozdowska^c, Agnieszka Wróbel-Tałaaj^c, Cezary Parzych^d, Artur Ratkiewicz^d, Beata Kolesińska^e, Heba A. Abd El-Razik^a and Farid S. G. Soliman^a

^aDepartment of Pharmaceutical Chemistry, Faculty of Pharmacy, Alexandria University, Alexandria, Egypt; ^bDepartment of Medical Biochemistry, Faculty of Medicine, Alexandria University, Alexandria, Egypt; ^cDepartment of Organic Chemistry, Medical University of Białystok, Białystok, Poland; ^dDepartment of Physical Chemistry, University of Białystok, Institute of Chemistry, Białystok, Poland; ^eInstitute of Organic Chemistry, Lodz University of Technology, Lodz, Poland

ABSTRACT

In light of searching for new breast cancer therapies, DNA-targeted small molecules were rationally designed to simultaneously bind DNA and inhibit human dihydrofolate reductase (*h*DHFR). Fourteen new arylidene-hydrazinyl-1,3-thiazoles (**5–18**) were synthesised and their dual DNA groove binding potential and *in vitro* *h*DHFR inhibition were performed. Two compounds, **5** and **11**, proved their dual efficacy. Molecular docking and molecular dynamics simulations were performed for those active derivatives to explore their mode of binding and stability of interactions inside DHFR active site. Anti-breast cancer activity was assessed for **5** and **11** on MCF-7 cells using **MTX** as reference. IC₅₀ measurements revealed that both compounds were more potent and selective than **MTX**. Cytotoxicity was examined against normal skin fibroblasts to examine safety and selectivity. Moreover, mechanistic studies including apoptosis induction and wound healing were performed. Further *in silico* ADMET assessment was conducted to determine their eligibility as drug leads suitable for future optimisation and development.

GRAPHICAL ABSTRACT



ARTICLE HISTORY

Received 11 January 2025
Revised 3 February 2025
Accepted 11 February 2025

KEYWORDS

Thiazoles; DHFR; DNA binders; anti-tumor; molecular modelling

Introduction

Cancer remains a growing health burden manifesting abnormal rapid uncontrolled cell division with multiple genetic alterations leading to abnormal cell growth, metastasis and drug resistance

with increased global mortality rates. Worldwide, an estimate of 20 million new cancer cases and nearly 10 million deaths from cancer were recorded in 2022. These statistics are expected to increase by ~77% till reaching 2050, thus causing further straining to the health systems and communities¹. Breast cancer, in particular, is

CONTACT Marwa H. El-Wakil ✉ marwa.elwakil@alexu.edu.eg Department of Pharmaceutical Chemistry, Faculty of Pharmacy, Alexandria University, Alexandria 21521, Egypt

Supplemental data for this article can be accessed online at <https://doi.org/10.1080/14756366.2025.2468353>.

© 2025 The Author(s). Published by Informa UK Limited, trading as Taylor & Francis Group.

This is an Open Access article distributed under the terms of the Creative Commons Attribution-NonCommercial License (<http://creativecommons.org/licenses/by-nc/4.0/>), which permits unrestricted non-commercial use, distribution, and reproduction in any medium, provided the original work is properly cited. The terms on which this article has been published allow the posting of the Accepted Manuscript in a repository by the author(s) or with their consent.

estimated to be the first or second leading cause of death in 95% of countries accounting for almost 80% of the death cases in low- and middle-income countries². While surgery or radiotherapy may provide adequate and quick intervention in early phases, yet conventional chemotherapy is still believed to be the most suitable treatment protocol for late stage breast cancer. Despite the wide range of approved anti-breast cancer medications with different mechanisms of action, their benefit is still a controversy limited by the poor selectivity, less efficacy, low safety profile, high toxicity and developed multi-drug resistance³. These issues urge the employment of breast cancer targeted therapy as an efficient approach to higher therapeutic potency and safety.

Advantageously, targeting a single biological molecule helps combat cancer with minimal risks of toxicity. Employing small molecule inhibitors that can tackle multiple simultaneous pathways of the same target biological molecule is considered a promising approach towards breast cancer treatment, helps circumvent the acquired drug resistance and contributes to successful management of cancer⁴. DNA is an important biological material and the main carrier of genetic information plays a pivotal role in maintaining structure of cells as well as controlling physiological

functions such as transcription, replication, and genetic information expression. DNA stands as a promising molecular cancer target for drug development. Small molecules that are able to cause DNA damage either through DNA groove-binding, direct intercalation of DNA strands, cross-linking or causing single (ssDNA)/double (dsDNA) strand breaks are considered valuable anticancer agents⁵. Direct DNA binding agents block cell division and force cancer cells to cell cycle arrest, apoptosis, and ultimately cell death⁶. The main pharmacophoric features that should be present in small molecule-DNA binders and necessary for direct DNA binding is the presence of planar aromatic/heterocyclic chromophore that are able to stack between DNA base pairs⁷. A number of cancer chemotherapeutic drugs such as doxorubicin (**DOX I**), daunorubicin **II**, mitoxantrone **III**, mitonafide **IV**, and amonafide **V** (Figure 1) primarily target the DNA through their planar aromatic anthracyclin/naphthalimide scaffolds causing intercalation between neighbouring base pairs⁸. Recently, much attention was paid towards studying the mechanisms of interaction of small-molecule DNA binders that greatly influences the design and synthesis of potential DNA-targeted drugs.

On the other side, target-specific DNA-synthesis inhibitors are appealing anticancer agents. A growing interest has been directed towards investigating human dihydrofolate reductase (hDHFR) enzyme which proved its indispensable role in nucleic acid precursors biosynthesis. DHFR is known to catalyse the reduction of dihydrofolate (DHF) to tetrahydrofolate (THF). This pathway is also coupled to thymidylate synthase (TS) which catalyses the reductive methylation of deoxyuridine monophosphate (dUMP) to deoxythymidine monophosphate (dTMP). Upon DHFR inhibition, intracellular reduced folate are depleted which are essential for one carbon transfer reactions involved in the synthesis of thymidylate, purine nucleotides, and related compounds vital for DNA, RNA, and protein biosynthesis⁹. Thus, inhibition of DHFR leads to disruption of DNA synthesis and death of proliferating cancer cells¹⁰. Methotrexate (**MTX; VI**), the well-studied prototype of classical DHFR inhibitors (Figure 2(A)), mainly used against non-small-lung cancer, breast cancer, non-Hodgkin's lymphoma and cancer of the head and neck, has faced several clinical utility problems owing to its poor cell penetration due to its hydrophilic glutamate side chain as well as dose-limiting toxicities that hampered its use¹¹. Other classical DHFR inhibitors include aminopterin (**AMT; VII**), edatrexate (**EDX; VIII**) and pralatrexate (**PDX; IX**). While non-classical DHFR inhibitors (Figure 2(B)), such as trimethoprim (**TMP; X**), trimetrexate (**TMQ; XI**), piritrexim (**PTX; XII**) and pyrimethamine **XIII** are much

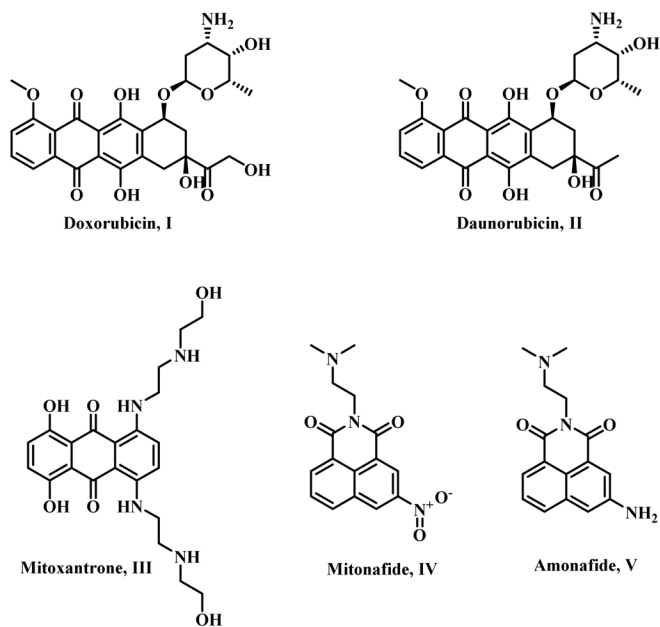


Figure 1. DNA targeting chemotherapeutic agents.

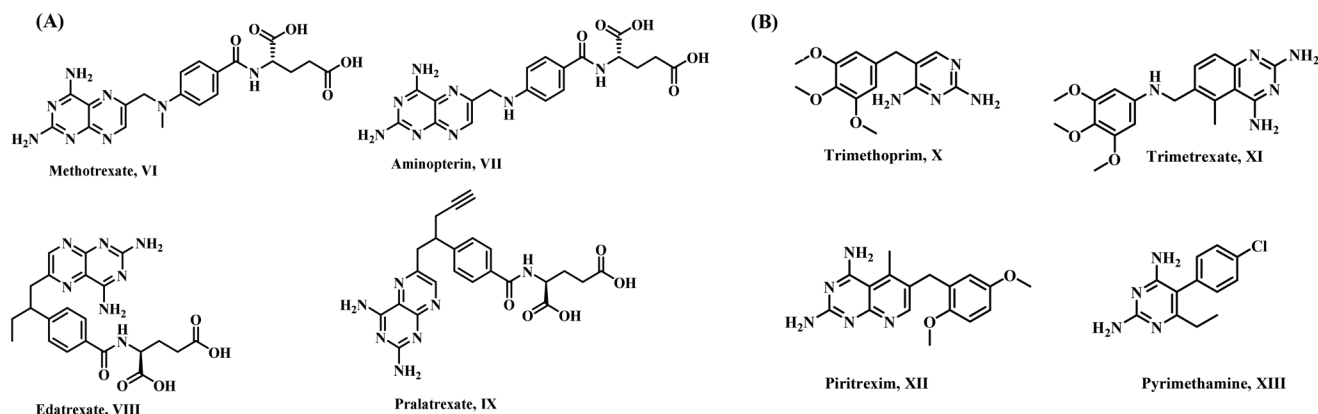


Figure 2. Selected examples of (A) classical and (B) non-classical DHFR inhibitors.

preferred due to their lower acquired resistance as they exhibit enhanced passive diffusion transport into cancerous cells owing to the present lipophilic side chains, thus providing selective treatment over classical antifolates¹².

Thiazole heterocycles have gained much attention owing to their privileged broad spectrum polypharmacologic applications including antitumor activities¹³. A number of thiazole-containing drugs such as dasatinib **XIV** and dabrafenib **XV** are recognised as promising antitumor agents¹⁴. Arylidene-hydrazinyl-thiazole is an interesting framework that proved efficacy to intercalate DNA and cause DNA damage. Synthesized pyridine-thiazole **XVI** was found to bind most effectively with DNA as groove binder *via* non-covalent binding interactions¹⁵. Whereas, furyl-thiazole hybrid **XVII** was reported to exhibit broad spectrum antitumor activity with high DNA binding affinity and cause dsDNA breaks confirmed by fluorescence and UV-Vis absorption measurements¹⁶. A reported study described newly synthesised thiazole-indole conjugates **XVIIIa** and **XVIIIb** showing the highest DNA binding affinity to the minor groove at A-T rich regions¹⁷. Whereas, a new hydrazonoquinoline-thiazole hybrid **XIX** showed its affinity against calf thymus DNA (ctDNA) as a potential DNA groove binder¹⁸ (Figure 3(A)).

Moreover, from the diverse scaffolds explored as DHFR inhibitors^{19–28} unfused thiazole-based derivatives are less investigated as non-classical DHFR inhibitors (Figure 3(B)), for instance; tiazoferin **XX** and thia-netropsin **XXI** were identified as non-classical DHFR inhibitors besides their DNA binding potential²⁹. It was recognised from previously reported molecular modeling studies that either aliphatic or aromatic substituents pendent to thiazole ring is essential for affinity within the active site of DHFR with remarkable inhibitory activity²³. From extensive literature survey, it was found that a 2-(4-methyl-thiazolyl)thio-6-substituted-quinazolin-4-one analogue **XXII** displayed potential DHFR inhibitory activity as an antitumor compound²⁵. A thioureido-1,3-thiazole analogue **XXIII** possessed an $IC_{50} = 0.05 \mu M$ against DHFR²². Also, 5-aryazo-2-hydrazonothiazoles **XXIVa–c** showed remarkable DHFR inhibitory activity in the range 0.042–0.701 μM ³⁰.

In view of the above-mentioned findings and in continuation to our anticancer program long established in our laboratory^{31–36} and to the previous interest in DNA binding agents^{16,37} and non-classical DHFR inhibitors^{12,38,39}, this work aims at targeting DNA *via* small-molecule antitumor agents as direct DNA binders augmented with non-classical antifolate activity for breast cancer

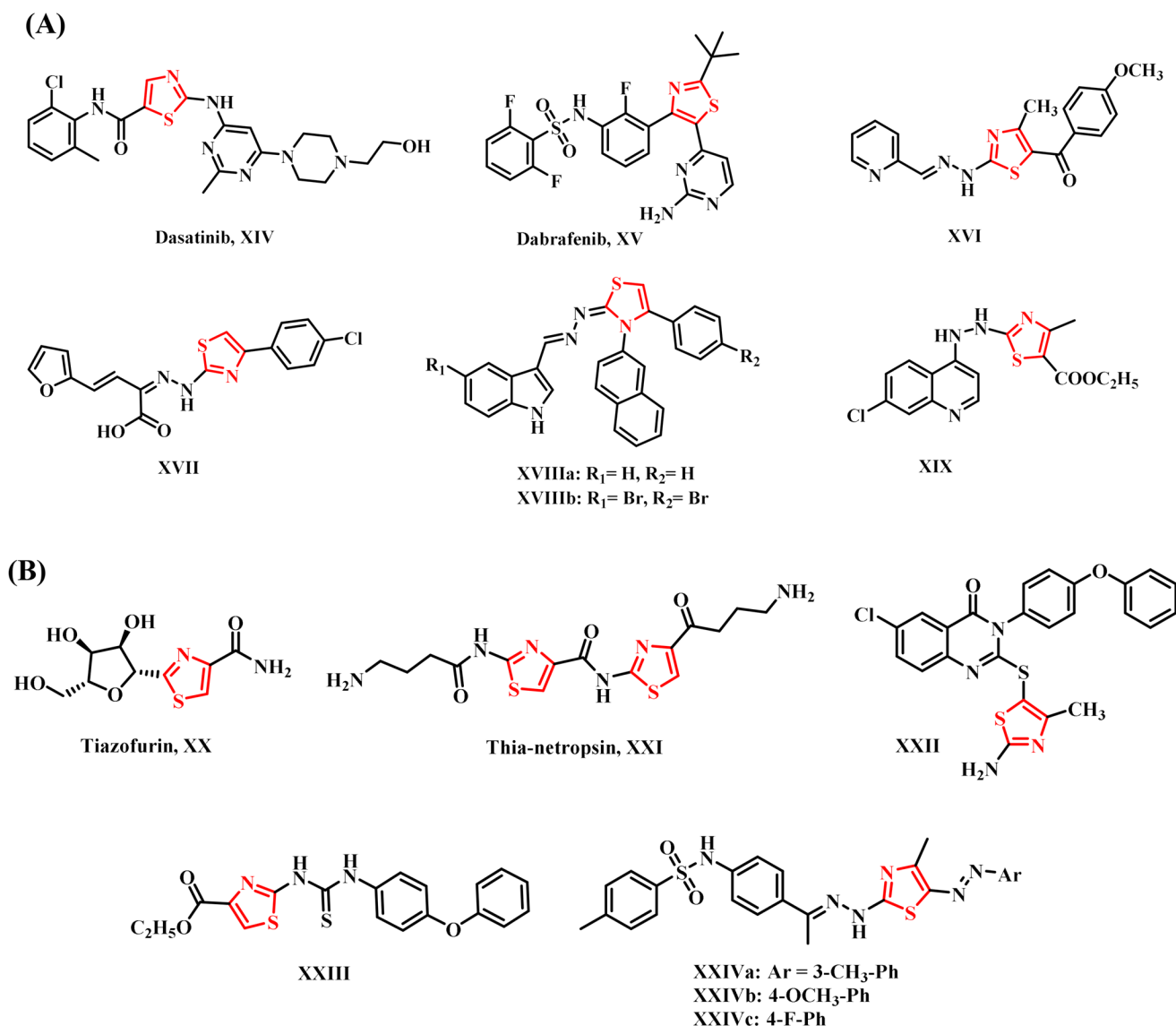


Figure 3. Illustrative examples for (A) thiazole-containing DNA binders and (B) thiazole-based DHFR inhibitors.

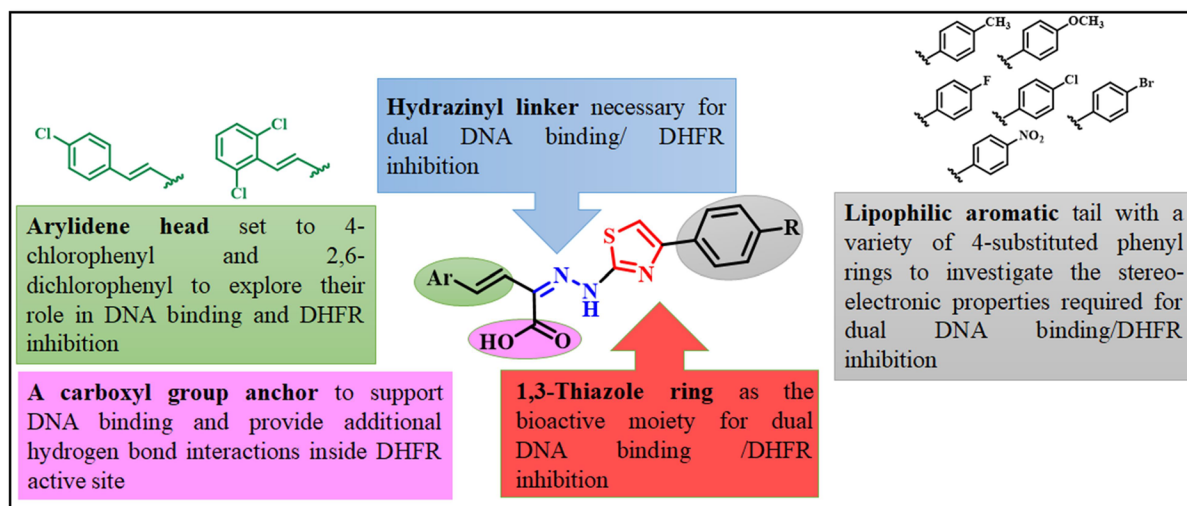


Figure 4. Illustrative strategy employed for the design of the new target derivatives.

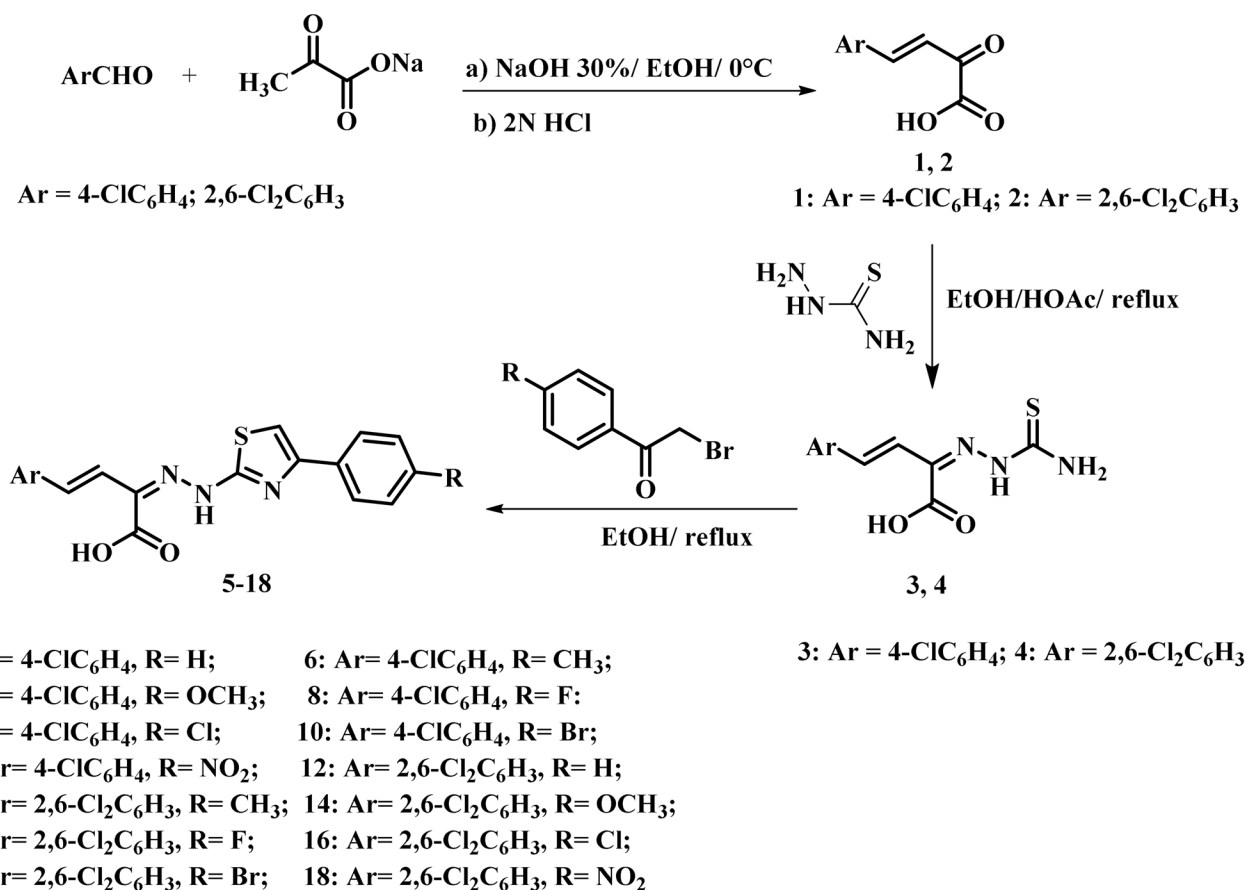
therapy. The novel series of compounds are designed to possess arylidene-hydrazinyl-1,3-thiazole scaffold, where this chromophore is anticipated to possess dual DNA-binding properties and antifolate potential as present in **XVI**, **XVII**, and **XXIVc**. This scaffold is anchored to a carboxyl moiety as well as tethered to a lipophilic aromatic tail enriched with a variety of electronic environment groups to confer DNA sequence selectivity at the proper sites as well as explore their influence on DHFR receptor binding at the active site. While the arylidene head was set to new aromatic groups, analogous to pyridyl, furyl, and phenyl groups of respective **XVI**, **XVII**, and **XXIVc**, to be 4-chlorophenyl and 2,6-dichlorophenyl moieties in order to comparatively assess the effect of *ortho* and *para* substitution pattern on both DNA binding potential and DHFR inhibitory potency (Figure 4). Structures of the synthesised derivatives were confirmed by different spectroscopic techniques involving FT-IR, ^1H NMR, ^{13}C NMR, and HRMS. The compounds were then biologically evaluated for their dual DNA binding potential and DHFR inhibition. For the most active compound(s), *in vitro* antitumor evaluation was investigated using MTT assay against breast (MCF-7) cancer cell line in reference to normal human skin fibroblast cells, as well as exploring the underlying antitumor mechanism of action including apoptosis induction and wound healing assay. Additional computational studies including molecular docking simulation and molecular dynamics investigation were performed, besides physicochemical and ADMET parameters assessment to identify their underlying lead and drug-like properties for further optimization and development.

Results and discussion

Chemistry

The designed compounds were synthesised adopting the synthetic routes depicted in Scheme 1. Precursors 2-oxobut-3-enoic acids **1** and **2** were prepared by reacting the appropriate benzaldehyde derivative with sodium pyruvate under Claisen–Schmidt conditions³⁷ in good yields and high purity. Thiosemicarbazones **3** and **4** were prepared by heating the respective precursors **1** and **2** with thiosemicarbazide in a mixture of aqueous ethanol and glacial acetic acid. Concerning FT-IR spectrum of compound **4**, the appearance of new absorption bands attributed to N=C=S

functionality at ν 1391, 1219, 963 cm^{-1} and NH_2 functionality at ν 3424, 3300 cm^{-1} confirmed formation of the desired product.¹H NMR spectrum of **4** revealed signals due to NH_2 protons at the expected chemical shift, in addition to signals due to NH proton at δ 11.36 ppm and COOH proton at δ 12.31 ppm. ^{13}C NMR, proton decoupled, spectrum of **4** revealed all carbons at their expected chemical shifts, with the characteristic carbon signals of carboxylic C=O carbon at δ 163.66 ppm and C=S at δ 178.44 ppm. Literature reports revealed that reaction of thiosemicarbazones with phenacyl bromides is usually carried out in ethanol/sodium acetate⁴⁰ or dioxane/trimethylamine⁴¹ mixtures. In the present investigation, the target thiazole derivatives **5–18** were obtained by heating the thiosemicarbazones **3** and **4** with the appropriate phenacyl bromides in absolute ethanol without the need of a base according to a previously reported procedure³⁵. Validation of the chemical structure of the obtained compounds was performed *via* FT-IR and NMR spectra. All compounds showed the broad band of carboxylic OH functionality in the range ν 3500–3000 cm^{-1} . Also, absorption bands attributed to NH functional group appeared in the range ν 3198–3118 cm^{-1} . The compounds lacked the absorption bands of C=S and NH_2 functionalities and instead revealed absorption bands of C–S–C functionality in the range ν 1343–1237 and 1060–1021 cm^{-1} . Compounds **11** and **18** showed frequency bands due to NO_2 group at ν 1557–1548 and 1341–1340 cm^{-1} . Further structure confirmation of the target compounds was done using NMR spectroscopy (Supplemental material Figures 1S–30S) and HRMS (Supplemental material Figures 31S–44S). Inspection of ^1H NMR spectra of **5–18** revealed signals attributed to aromatic, ethenyl, and C_5 -thiazole protons at their predicted chemical shifts. Signals attributed to carboxylic OH proton appeared in some derivatives and were offset in others. Additional signals of CH_3 protons were observed for derivatives **6** and **13** at δ 2.31 ppm (Supplemental material Figures 5S, 19S). While compounds **7** and **14** showed signals attributed to OCH_3 protons at δ 3.77 and 3.86 ppm, respectively (Supplemental material Figures 7S, 21S). In ^{13}C NMR, all carbon signals appeared at their expected chemical shifts. Compounds **6** and **13** showed a signal at δ 20.86 ppm due to CH_3 carbon (Supplemental material Figures 6S, 20S) while derivatives **7** and **14** displayed a signal at δ 55.19 ppm due to OCH_3 carbon (Supplemental material Figures 8S, 22S).



Scheme 1. Synthetic steps for the preparation of the target thiazole derivatives **5–18**.

Table 1. DNA-binding effects and hDHFR inhibitory potential for the new analogues **5–18** in reference to **NT**, **TMP**, **MTX**, and **DOX**.

No.	Decrease in fluorescence (%)					hDHFR IC ₅₀ (μM)
	pBr322	Calf Thymus DNA	T4 DNA	Poly (dA-dT) ₂	Poly (dG-dC) ₂	
EtBr	100	100	100	100	100	–
5	63.44	63.15	28.05	56.91	67.28	0.08 ± 0.001
6	43.72	46.31	51.22	60.89	73.39	48.23 ± 0.002
7	62.36	44.21	36.58	49.18	62.38	39.41 ± 0.030
8	60.93	40.00	37.19	52.83	62.99	10.51 ± 0.050
9	53.40	53.68	50.00	71.19	49.23	36.18 ± 0.010
10	53.76	30.53	32.32	39.34	50.15	58.29 ± 0.020
11	56.21	46.31	28.89	53.39	56.57	0.06 ± 0.030
12	54.84	60.53	48.17	54.80	59.37	21.06 ± 0.020
13	62.01	67.71	51.22	55.74	75.62	18.06 ± 0.030
14	51.61	58.95	40.85	67.21	61.25	31.02 ± 0.040
15	70.97	72.10	39.02	55.27	57.81	62.31 ± 0.020
16	64.16	50.53	52.44	51.29	63.12	53.18 ± 0.010
17	61.65	54.21	35.36	42.62	63.44	60.28 ± 0.020
18	55.56	76.84	45.12	37.00	62.50	63.18 ± 0.010
NT	74	90.24	70.06	62.02	85.13	n.d
MTX	100	n.d	n.d	n.d	n.d	0.08 ± 0.030
TMP	100	n.d	n.d	n.d	n.d	55.26 ± 0.010
DOX	100	n.d	n.d	n.d	n.d	8.31 ± 0.060

n.d = not determined.

Bold values are indicated for the potent derivatives.

Biological evaluation

DNA-binding effects using ethidium bromide assay

For all newly target compounds, an ethidium bromide (EtBr) test was performed on various plasmid DNAs. The ethidium–DNA complex is considered a well-studied experimental prototype

employed in the comparison of small molecule interactions with nucleic acids. EtBr exhibits fluorescence enhancement upon binding to intact DNA. However, any damage occurring to DNA strands by the effect of small molecule DNA binders will cause decrease in the fluorescence intensity⁴². Results are presented (Table 1) as the percentage decrease in fluorescence of each substance relative to netropsin (**NT**), a standard compound that binds inside the minor groove. The degree of EtBr displacement from the complex with plasmid pBR322 for **NT** under the same conditions was 74%⁴³. Significantly, all target compounds had greater binding strength to plasmid pBR322 than **NT**. Compound **6** had the lowest value of the degree of displacement of EtBr (43.72%), while **15** possessed the highest one (70.97%). However, from the data obtained, it is not possible to observe a structure–activity relationship, and to determine which structural factors affect it. The values for all compounds are quite similar, and the only certainty is that all derivatives bind to DNA. Additionally, we can learn more about the properties of the new derivatives from a study of the displacement of EtBr from its complexes with calf thymus DNA, T4 coliphage DNA, poly(dA-dT)₂, and poly(dG-dC)₂. Calf thymus DNA is a natural DNA widely used in studying DNA binding of anticancer agents. In this study against calf thymus, the tested compounds proved to be more active than **NT** with values for the degree of displacement of EtBr ranging from 30.53% to 76.84%, compared to 90.24% for **NT**. Furthermore, all derivatives tested bind to T4 coliphage DNA better than **NT**. T4 coliphage DNA is glycosylated throughout the major groove⁴⁴, thus, complexing of new compounds by T4 DNA should only occur in the minor groove. Results for derivatives **5–18** gave evidence of their minor-groove selectivity, especially for compounds

5 and **11**, where the percentage of decrease of fluorescence was 28.05% and 28.89%, respectively.

Our study indicated that compounds **5–18** had interacted with AT as well as GC-base pairs and we can observe the greatest preference for AT-base pairs only of three compounds: **9**, **14**, and **18**. The last one showed 37.00% decrease of fluorescence compared to **NT** (62.02%). Other compounds bound to GC-rich sequences stronger than **NT** (85%) with compounds **9** (49.23%) and **10** (50.15%) showing the lowest decrease in fluorescence intensity.

Dihydrofolate reductase inhibition

After proving their DNA binding potential, all target compounds **5–18** were then evaluated for their inhibitory potency against *h*DHFR enzyme using a reported procedure of recombinant human DHFR enzyme³⁸ employing **MTX**, **TMP**, and **DOX** as positive controls (Table 1). It was observed that most compounds namely **5–9**, **11–14**, and **16** showed better inhibitory activity with IC_{50} values ranging from 0.06–53.18 μ M compared to **TMP** (IC_{50} = 55.26 μ M). Derivative **5** was equipotent to **MTX** with IC_{50} = 0.08 μ M, whereas, compound **11** (IC_{50} = 0.06 μ M) showed better inhibitory activity compared to **MTX**. Nevertheless, both **5** and **11** were more potent against *h*DHFR than **DOX** (IC_{50} = 8.31 μ M). In an attempt to outline a preliminary structure–activity relationship for these derivatives, it was observed that in general those derivatives having the 4-chlorostyryl head (**5–11**), except for derivative **10**, showed good DHFR inhibitory activity (IC_{50} = 0.06–48.23 μ M) more potent than **TMP** (IC_{50} = 55.26 μ M). Interestingly, two compounds **5** and **11** displayed potent inhibitory activity as evident from their IC_{50} values compared to reference drugs **TMP** and **MTX**. While the other derivatives possessing the 2,6-dichlorostyryl moiety (**12–18**) showed relatively moderate to weak inhibitory activity (IC_{50} = 18.06–63.18 μ M), with only four compounds **12–14** and **16** (IC_{50} = 18.06–53.18 μ M) showing better activity than **TMP** but none was even equipotent to **MTX**. As for derivatives **5–11**, it could be noticed that compounds having electron-withdrawing groups in the terminal phenyl ring pendent to the thiazole nucleus displayed better activity than those possessing electron donor groups and are in the following descending order of activity: **11** (R=NO₂) > **8** (R=F) > **9** (R=Cl) > **10** (R=Br). This could point out to the significance of the size of the electronegative atom with respect to DHFR inhibitory activity, where small-sized atoms as N of NO₂ group and F atom revealed better activity than large-sized Cl and Br halogen atoms, respectively. However, this conclusion could not be drawn for the series of compounds **12–18**.

Molecular docking

Binding mode analysis. Molecular docking is considered an outstanding way to study molecular interactions between small molecule inhibitors and their anticipated targets inside the active binding site⁴⁵. In this work, molecular docking analysis was employed for all new 14 ligands **5–18** against *h*DHFR enzyme. The binding free energy (Kcal/mol) was calculated for all ligands and compared to the obtained *h*DHFR IC_{50} values (Table 2). It was found that the binding energy values between the thiazole derivatives and the protein are similar, with the lowest being –9.963 kcal/mol for compound **18** and the highest being –9.601 kcal/mol for compound **5**, and these values are close to those of **DOX**. Additionally, the binding energies for the tested compounds are lower than those for **MTX** and significantly lower than those for **TMP**. Taking into consideration that **5** and **11** exhibited the lowest IC_{50} values against *h*DHFR, they were selected

Table 2. Comparison of the IC_{50} values (μ M) with the most advantageous ligand-protein binding free energy values (kcal/mol).

Ligand	Binding energy (kcal/mol)	IC_{50} (μ M)
5	–9.601	0.08 ± 0.001
6	–9.814	48.23 ± 0.002
7	–9.732	39.41 ± 0.030
8	–9.801	10.51 ± 0.050
9	–9.747	36.18 ± 0.010
10	–9.789	58.29 ± 0.020
11	–9.883	0.06 ± 0.030
12	–9.73	21.06 ± 0.020
13	–9.878	18.06 ± 0.030
14	–9.827	31.02 ± 0.040
15	–9.893	62.31 ± 0.020
16	–9.818	53.18 ± 0.010
17	–9.878	60.28 ± 0.020
18	–9.963	63.18 ± 0.010
MTX	–9.296	0.08 ± 0.030
TMP	–7.553	55.26 ± 0.010
DOX	–9.726	8.31 ± 0.060

for further studies alongside compound **18** which showed weak inhibitory potency yet demonstrated the highest binding free energy with the protein. The analysis also encompassed the quantity and varieties of interactions between the chosen ligands and the reference drugs **MTX**, **TMP** and **DOX** with *h*DHFR following their docking into the protein (Figure 5).

Hydrophobic interactions were detected between the protein and the examined ligands following docking procedure. Notably, compounds **5**, **11**, and **18** exhibited prominent interactions with residue Lys55. Alongside the hydrophobic interaction with the aromatic ring, Lys55 also engages in π -cationic interactions with the thiazole ring. These rings are interconnected, facilitating their interactions with Lys55. For ligand **5**, unfavourable donor–donor and acceptor–acceptor interactions were observed. Compound **11**, on the other hand, engages in π - π T-shaped interactions with residue Phe34. Similar interactions are observed with **DOX**, involving the same residue. In contrast, π - π stacked interactions were noted with **TMP** aromatic ring. Carbon–hydrogen bonds are formed by all reference ligands, while conventional hydrogen bonds are formed by the analysed compounds (Table 3).

The highest number of hydrogen bonds was observed with **MTX**. Of particular importance is the bond with Glu30³⁸. This type of bond is also observed in **TMP**, where it forms with the involvement of the ligand's amino group. Although this group is also present in **DOX** molecule, no interaction between **DOX** and Glu30 has been observed. Since the amino group is absent in thiazole ligand molecules, a H–bond between Glu30 and these ligands was not observed. **DOX** forms hydrogen bonds with Ser59 and Tyr121. The bond with Ser59 is also observed in ligand **5** (where it is the only hydrogen bond involving the ligand's carboxyl group) and ligand **11** (which also involves the carboxyl group of the compound). In addition to the hydrogen bond with Ser59, ligand **11** also forms a bond with Ser119. The same bond with Ser119 is present with ligand **18**. The formation of this bond in both **11** and **18** is probably due to the presence of a nitro group in these compounds. Additionally, ligand **18** forms a hydrogen bond with Asp21 via its hydroxyl group. However, lack of bonding with Ser59 might explain the weak affinity of **18** to *h*DHFR in terms of IC_{50} value. The ligand seems to bind tightly in a neighbouring area to the active binding site. Thus, based on the hydrogen bonding information, it can be inferred that the active thiazole ligands **5** and **11** bind differently from that of **MTX** and **TMP** but may be similar to that of **DOX**.

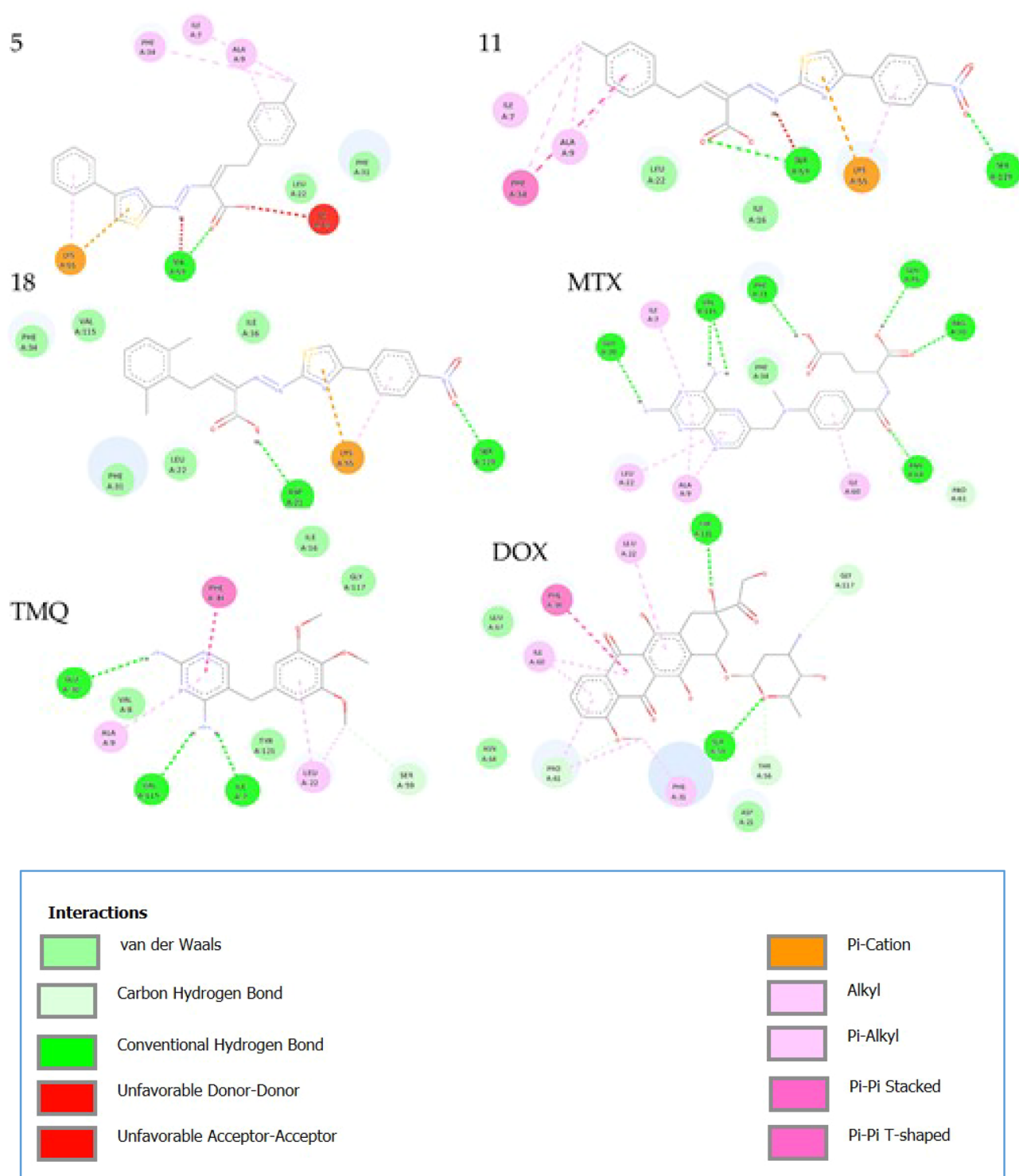


Figure 5. 2D representations illustrating ligand-protein interactions for compounds **5**, **11**, and **18** in reference to **MTX**, **TMP**, and **DOX**.

Molecular docking statistics. For statistical analysis of the molecular docking outcomes, a variable window docking approach was implemented for compounds **5**, **11**, **18**, and **DOX**. A conformation refers to a different spatial arrangement of the same molecule. We only considered positions where the binding energy was stronger than -9kcal/mol . The number of conformations found for **5**, **11**, **18**, and **DOX** were 154, 187, 217, and 145, respectively. Analysis of the variable window docking results indicated that **DOX** formed the fewest systems with energies below -9kcal/mol . However, all these

configurations fall into a single category, unlike the thiazole ligands, which are assigned to five positions each (Table 4). This suggests that **DOX's** interactions with the protein are more restricted by its conformation, allowing it to bind to *h*DHFR in fewer ways compared to ligands **5**, **11**, and **18**. Five positions were identified for each of the selected thiazole ligands, while one position was determined for reference ligand **DOX**, all of which were analysed (Tables 5 and 6).

DOX at position #1 shows an affinity with a median value of -9.694kcal/mol . The binding strength ranges from a minimum of

Table 3. Description of conventional hydrogen bonds formed by derivatives **5**, **11** and **18** and reference ligands with hDHFR.

Ligand	Residue	Description of a hydrogen bond
5	Ser59	Bond to C=O group in ligand's carboxyl group
11	Ser59	Bond to C=O group in ligand's carboxyl group
	Ser119	Bond to the ligand's -NO ₂ group
18	Asp21	Bond to -OH group in ligand's carboxyl group
	Ser119	Bond to the ligand's -NO ₂ group
MTX	Glu30	Bond to the ligand's -NH ₂ group
	Phe31	Bond to -OH group in ligand's carboxyl group
	Glu35	Bond to -OH group in ligand's carboxyl group
	Asp64	Bond to the C=O group in the ligand's amide group
	Arg70	Bond to C=O group in ligand's carboxyl group
	Val115	Bond to the ligand's -NH ₂ group
TMP	Ile7	Bond to the ligand's -NH ₂ group
	Glu30	Bond to the ligand's -NH ₂ group
	Val115	Bond to the ligand's -NH ₂ group
DOX	Ser59	Bond to the oxygen atom in the ligand ring
	Tyr121	Bond to the ligand's -OH group

−9.799 kcal/mol to a maximum of −9.044 kcal/mol. This trend is statistically significant; with a p value < 0.05. Position #1 is the most frequently occupied position by the ligands, also representing the conformation with the lowest median energy. The Kruskal–Wallis test was utilised to compare these positions and the primary conclusions are as follows:

- Position #1: The energies of thiazole ligands **5**, **11**, and **18** differ significantly from the energy of **DOX** ($p < 0.05$). This means their binding strengths are statistically different.
- Position #2: The energies of ligands **5** and **11** at position #2 are statistically similar ($p > 0.05$). The same goes for ligands **5** and **18**, but the median energies of ligands **11** and **18** are statistically different from each other ($p < 0.05$). Additionally, the medians of these thiazole ligands are statistically different from **DOX** at position #1 ($p < 0.05$).

Table 4. Ligands **5**, **11**, and **18** positions obtained after docking with variable window.

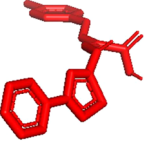
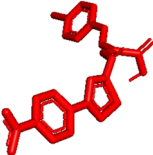
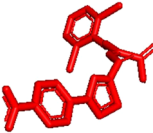
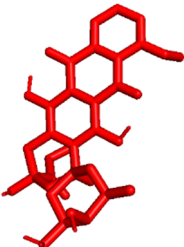
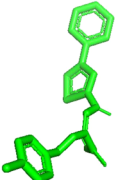
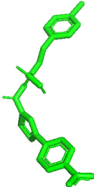
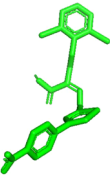
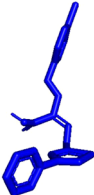
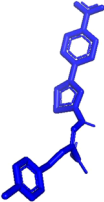
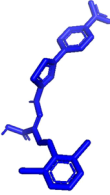
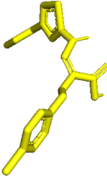

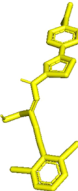
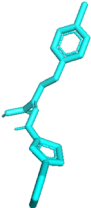
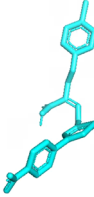
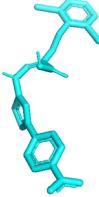
	5	11	18	DOX
Position 1				
Position 2				
Position 3				
Position 4				
Position 5				

Table 5. Abundance and percentage of occurrence of individual positions of ligands **5**, **11**, and **18**.

	5	11	18
Position #1	123 (79.87%)	81 (43.32%)	92 (42.40%)
Position #2	7 (4.54%)	74 (39.57%)	37 (17.05%)
Position #3	19 (12.34%)	9 (4.81%)	30 (13.82%)
Position #4	4 (2.60%)	10 (5.35%)	50 (23.04%)
Position #5	1 (0.65%)	13 (6.95%)	8 (3.69%)

Table 6. Median values of protein-ligand binding energy (kcal/mol) calculated for the individual positions of ligands **5**, **11**, and **18**.

	5	11	18
Position #1	−9.615 −9.688/−9.049 $p < 0.05$	−9.85 −9.936/−9.077 $p < 0.05$	−9.948 −10.18/−9.662 $p < 0.05$
Position #2	−9.321 −9.369/−9.187 $p > 0.05$	−9.5685 −9.656/−9.426 $p < 0.05$	−9.443 −9.608/−9.367 $p > 0.05$
Position #3	−9.298 −9.336/−9.228 $p < 0.05$	−9.437 −9.458/−9.374 $p > 0.05$	−9.247 −9.334/−9.178 $p > 0.05$
Position #4	−9.1125 −9.139/−9.058 $p > 0.05$	−9.4045 −9.436/−9.302 $p > 0.05$	−9.117 −9.181/−9.001 $p < 0.05$
Position #5	−9.025 ^a – –	−9.366 −9.397/−9.328 $p > 0.05$	−9.0445 −9.119/−9.008 $p > 0.05$

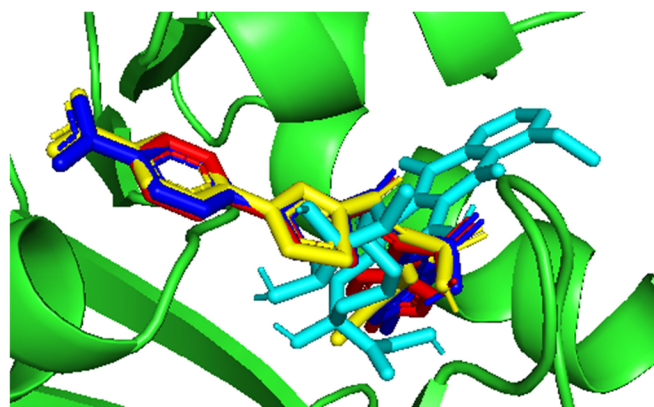
^aOnly a single energy value is provided for position #5 of ligand **5**, indicating that only one corresponding conformation was identified. For the remaining combinations, the minimum and maximum energy values (min/max) are also provided. To evaluate the normality of the energy distributions, the Shapiro–Wilk test was conducted, with $p \leq 0.05$ indicating a non-normal distribution and $p \geq 0.05$ indicating a normal distribution.

- Position #3: The energies of the thiazole ligands at position #3 are statistically similar to each other ($p > 0.05$). However, there is statistically significant difference between the energies of all thiazole ligands at pose #3 and **DOX** at position #1 ($p < 0.05$).
- Position #4: There is no statistical difference between energies of the thiazole ligands at position #4 ($p > 0.05$). However, they differ from the energy of **DOX** at position #1 ($p < 0.05$).
- Position #5: The median energy of ligand **11** at pose #5 is statistically similar to ligand **18** at the same pose ($p > 0.05$). However, the affinities of both ligands **11** and **18** at position #5 are statistically different from that of **DOX** at position #1 ($p < 0.05$).

In conclusion, the energy of **DOX's** position #1 is statistically different from the positions of the other thiazole ligands due to **DOX's** wide energy range (−9.799 to −9.044 kcal/mol). The higher energy positions of the thiazole ligands (positions #3, #4, and #5) do not differ significantly from each other. However, the energies of position #1 for all these ligands are statistically significantly different from each other. This is due to their varied interactions with the protein, including the formation of hydrogen bonds with different residues and the presence or absence of donor–donor, donor–acceptor, or π – π interactions. The structures of the ligands with the lowest energy are presented in Figure 6.

Molecular dynamics simulation

20 ns molecular dynamics simulations were performed for thiazole ligands: **5**, **11**, and **18** together with three reference ligands: **MTX**, **TMP**, and **DOX**, as well as for the apoenzyme. To assess the stability of each system, the following parameters were analysed: root mean

**Figure 6.** Ligand structures: **5** (red), **11** (blue), **18** (yellow), and **DOX** (cyan) with the lowest energy docked in hDHFR (green).

square deviation (RMSD), root mean square fluctuation (RMSF), solvent accessible surface area (SASA), and radius of gyration (Rg). An analysis of the hydrogen bonds that formed between the ligand and the protein during the simulation was also conducted.

Analysis of the simulation parameters. The relationship between the mentioned parameters (RMSD, RMSF, SASA, and Rg) and simulation time or residue for the three thiazole ligands, reference ligand **DOX**, and an apoenzyme is depicted in Figure 7. RMSD illustrates the stability of protein backbone upon interaction with the tested ligands. At the beginning of the simulation, RMSD values for ligand **5** are smaller than those for the apoenzyme but larger than for other analysed systems. As the simulation progresses, around 7 ns forward, these values become comparable to those for both the apoenzyme and ligand **11**, slightly exceeding those for **DOX**. In contrast, initial RMSD values for compound **11** are relatively large but comparable to the apoenzyme, diminishing over time. By approximately 7 ns, RMSD values for **11** align with those for **18** and **DOX**, significantly smaller than for **5** and the apoenzyme. Subsequently, RMSD for **11** undergoes slight increments, matching other systems except for **18**, which remains lower. For compound **18**, initially, RMSD values are comparable to those for ligand **11** and **DOX** but smaller than those for **5** and the apoenzyme. These values then notably increase, remaining the highest until about 9 ns. Between 10 and 13 ns, RMSD for **18** closely mirrors that of **5**, before rising significantly and surpassing values for other systems. Considering the RMSD values, it can be inferred that potential inhibitors **5** and **11** exhibit a stabilising effect on hDHFR, comparable to or slightly weaker than that of **DOX**, while **18** demonstrates the least stabilising effect. Meanwhile, RMSF is a parameter that assesses the flexibility and rigidity of residues throughout the simulation. The RMSF parameter dependency graphs for all systems under study exhibit similar patterns. These graphs feature peaks where RMSF values for specific residues are notably higher compared to most amino acid derivatives. Ligand **5** demonstrates consistently moderate RMSF values during peak occurrences, indicating its effective stabilisation of the protein. In contrast, the complex with **11** shows slightly elevated values, particularly noticeable for the Gly129 residue. However, for the majority of the simulation duration, the RMSF values for compound **11** do not significantly deviate from those of **DOX** or the apoenzyme. On the other hand, ligand **18** exhibits the weakest stabilising effect, evidenced by its consistently higher values during peaks for residues such as Lys18, Pro25, Glu143, Leu166, Ser167, and Asp168.

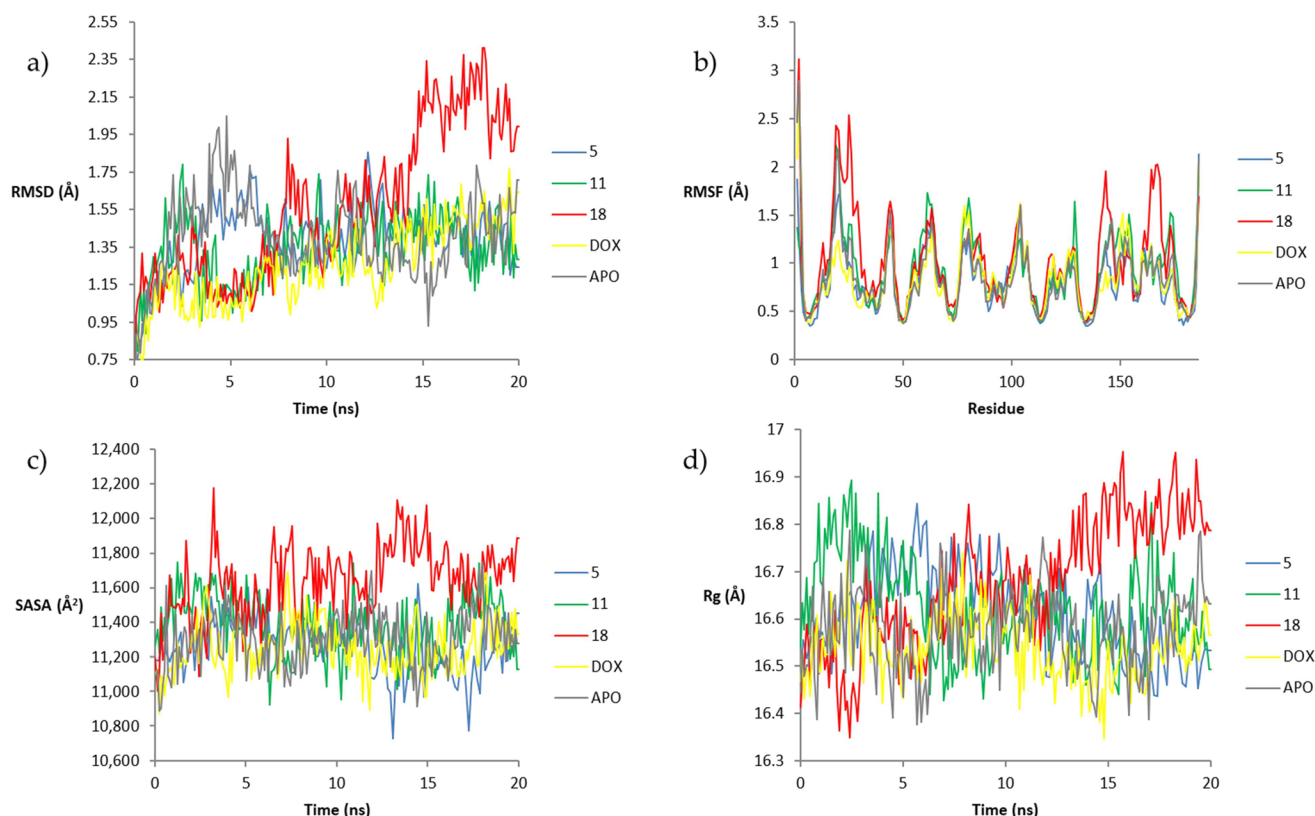


Figure 7. Plots of the dependence of (a) RMSD, (b) RMSF, (c) SASA, (d) Rg on simulation time and residue number for ligands: **5**, **11**, **18**, **DOX**, and apoenzyme.

Table 7. Hydrogen bonds formed between the ligand and the protein during the simulation including information about the donor/acceptor of these bonds (main – main chain, side – side chain) and the percentage of frames in which each bond occurs.

Ligand	Hydrogen bond donor	Hydrogen bond acceptor	Occupancy (%)
5	5 - Side	Ser59 - Side	18.45
	Arg70 - Side	5 - Side	2.30
11	Thr56 - Side	11 - Side	26.00
	11 - Side	Val155 - Main	1.00
	Phe31 - Side	11 - Side	1.00
18	18 - Side	Thr56 - Side	26.00
	18 - Side	Asp21 - Main	24.00
	18 - Side	Asp21 - Side	4.50
	18 - Side	Gly20 - Main	1.50
	18 - Side	Ser59 - Main	1.00
MTX	MTX - Side	Tyr121 - Side	20.00
	Leu22 - Main	MTX - Side	1.50
	MTX - Side	Ala9 - Main	1.00
	Ala9 - Main	MTX - Main	1.00
	MTX - Main	Gly20 - Main	1.00
TMP	TMP - Side	Ile7 - Main	33.50
	TMP - Side	Glu30 - Side	24.00
	TMP - Side	Val115 - Main	14.00
	Ser59 - Side	TMP - Side	3.00
DOX	DOX - Side	Glu30 - Side	36.00
	DOX - Side	Val115 - Main	27.50
	Thr56 - Side	DOX - Side	11.50
	DOX - Side	Gly20 - Main	2.00
	DOX - Side	Thr56 - Side	1.00

To further examine the tested ligands' complexes stability, SASA measurements were also considered. During the initial half of the simulation, potential inhibitor **5** exhibits low SASA, similar to that of the apoenzyme. In the latter half, these values further decrease, often becoming the lowest among the complexes analysed,

indicating the stabilising nature of this compound. Conversely, ligand **11** initially demonstrates relatively high SASA values for approximately the first 5 ns of the simulation. Subsequently, these values decrease and approach those of the apoenzyme, sometimes even becoming smaller, as well as **DOX**. On the other hand, **18** consistently displays the highest SASA values for the majority of the simulation duration, indicating its weak stabilising effect. Studying Rg imparts knowledge on the protein compactness. At the initial phase of the simulation, spanning up to approximately 4 ns, the Rg values for complex with **5** remain low, comparable to those of **DOX** and the apoenzyme, higher than ligand **18**, but lower than complex with **11**. Subsequently, up to about half of the simulation time, these values steadily rise, surpassing those of other systems except **18**. However, in the latter half of the simulation, these values decline, becoming lower than those of **11** and **18**, and comparable to, sometimes even lower than, those of the apoenzyme and **DOX**. Concerning Rg, inhibitor **5** seems to be the most effective in stabilising the complex with hDHFR. Conversely, Rg values for ligand **11** are highest among the tested systems during the initial 1/3 of the simulation time. However, in the later stages of the simulation, they decrease and become the lowest, eventually reaching comparability with the apoenzyme from about 10 ns onwards. Rg values increase again, remaining smaller only than those for ligand **18**. This indicates that the enzyme-stabilising properties of derivative **11** are weaker compared to for **5**. In contrast, Rg values for **18** start at their lowest point at the beginning of the simulation, but they began to rise from around 3 ns on. From approximately 13 ns until the simulation end time, they were the highest among all systems. Analysis of RMSD, RMSF, SASA, and Rg parameters allowed us to conclude that the stabilising effect on the enzyme decreases in the series: **5** > **11** > **18**. For ligand **5** it is better compared to **DOX**, for ligand **11** it is similar to **DOX**, and for compound **18** it is weaker than for **DOX**.

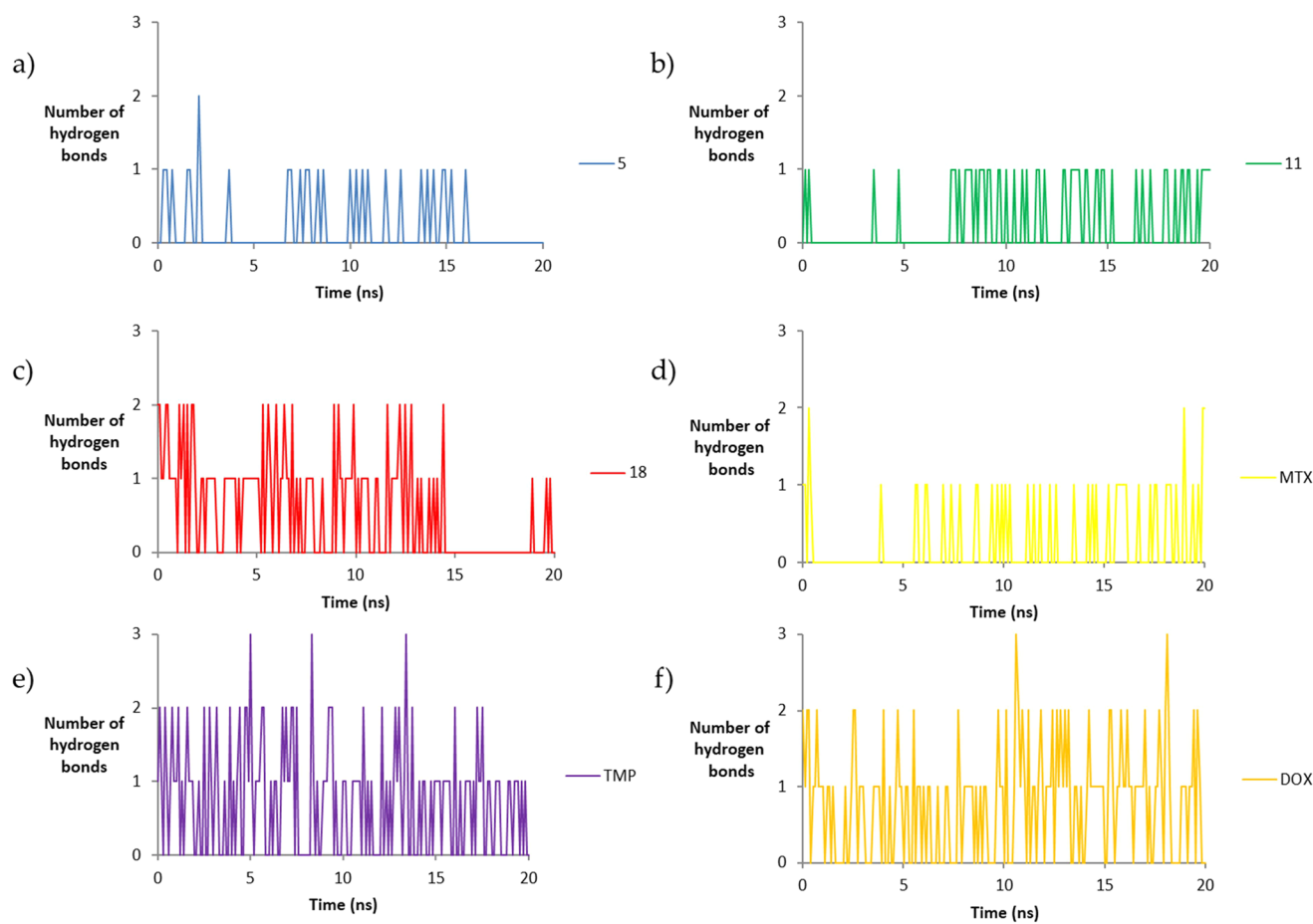


Figure 8. Dependence of the number of hydrogen bonds formed on simulation time for ligands: (a) **5**, (b) **11**, (c) **18** and reference ligands: (d) **MTX**, (e) **TMP**, (f) **DOX**.

Hydrogen bond analysis. The characteristics of the hydrogen bonds formed between the ligand and the protein during the simulation are shown in Table 7, and the dependence of the number of hydrogen bonds on the simulation time is shown in Figure 8. Compound **5** forms two hydrogen bonds with *h*DHFR, notably one with Ser59, as also observed in molecular docking analysis. This bond appears more frequently than the one with Arg70, which was not observed during docking. Throughout the simulations, **11** also establishes two hydrogen bonds, with the one involving the Thr56 residue being more prevalent in occurrence. Interestingly, this bond did not manifest during the docking phase. Among our proposed derivatives, **18** forms the highest number of hydrogen bonds, with the most significant ones with Asp21 and Thr56. The former bond was noted following the docking of this ligand into the protein. Comparatively, the reference drugs form a greater number of hydrogen contacts than the thiazole ligands. **MTX** and **TMP** predominantly bond with residues other than those engaged by **5**, **11**, and **18**, such as Glu30, Tyr121, and Ile7. Conversely, **DOX** forms hydrogen bonds with both distinct (e.g. Glu30, Val115) and overlapping residues (e.g. Thr56). Notably, a particularly significant contact with Glu30 was not observed for **MTX** during simulations but became evident after the ligand was docked. For **TMP** and **DOX**, this bond constitutes 24% and 36%, respectively. Its formation and frequent occurrence during simulation are attributed to the presence of the amino group. Additionally, **DOX**, alongside this interaction, forms bonds characteristic of thiazole ligands. Given the structural disparities between the reference drugs and **5**, **11**, and **18**, their mechanism of action may diverge. For

complexes formed by **5**, **11**, and **MTX**, a single hydrogen bond is most common during the entire simulation at any given time. In contrast, ligands **18**, **TMP**, and **DOX** are more likely to form two bonds compared to the rest of the systems studied. To gain further insights into the systems' stability during simulations, the distance between the centres of mass of the ligand and the amino acid with which it most often formed hydrogen bonds and the residuum of Glu30, commonly recognised⁴⁶ as one of the most important residues involved in the DHFR inhibition activity, were also analysed to determine the stability of the system (Figure 9). Throughout the vast majority of the simulation duration, the distance between ligand **5** and Ser59 remains the smallest compared to the reference ligands. Moreover, this value exhibits minimal variation, unlike the distances of ligands **11** and **18** from Thr56 and Asp21, respectively. Despite notable fluctuations for **11**, this distance consistently remains the lowest among the systems analysed for most of the simulation duration. Conversely, for compound **18**, the separation is comparable to that of the reference ligands for much of the simulation time. However, during some intervals such as 9–11 and 17–19 ns, this value is the smallest. These findings indicate a diminishing stabilising effect of the enzyme across the ligands: **5**, **11**, **18**, substantiating the conclusions drawn from the simulation parameter analysis. For the majority of the simulation duration, the distance between ligands **5**, **11**, and **18** and Glu30 is consistently greater compared to that of the reference ligands from this residue, except for **MTX**, for which the values are larger in some time intervals, but remain smaller in others.

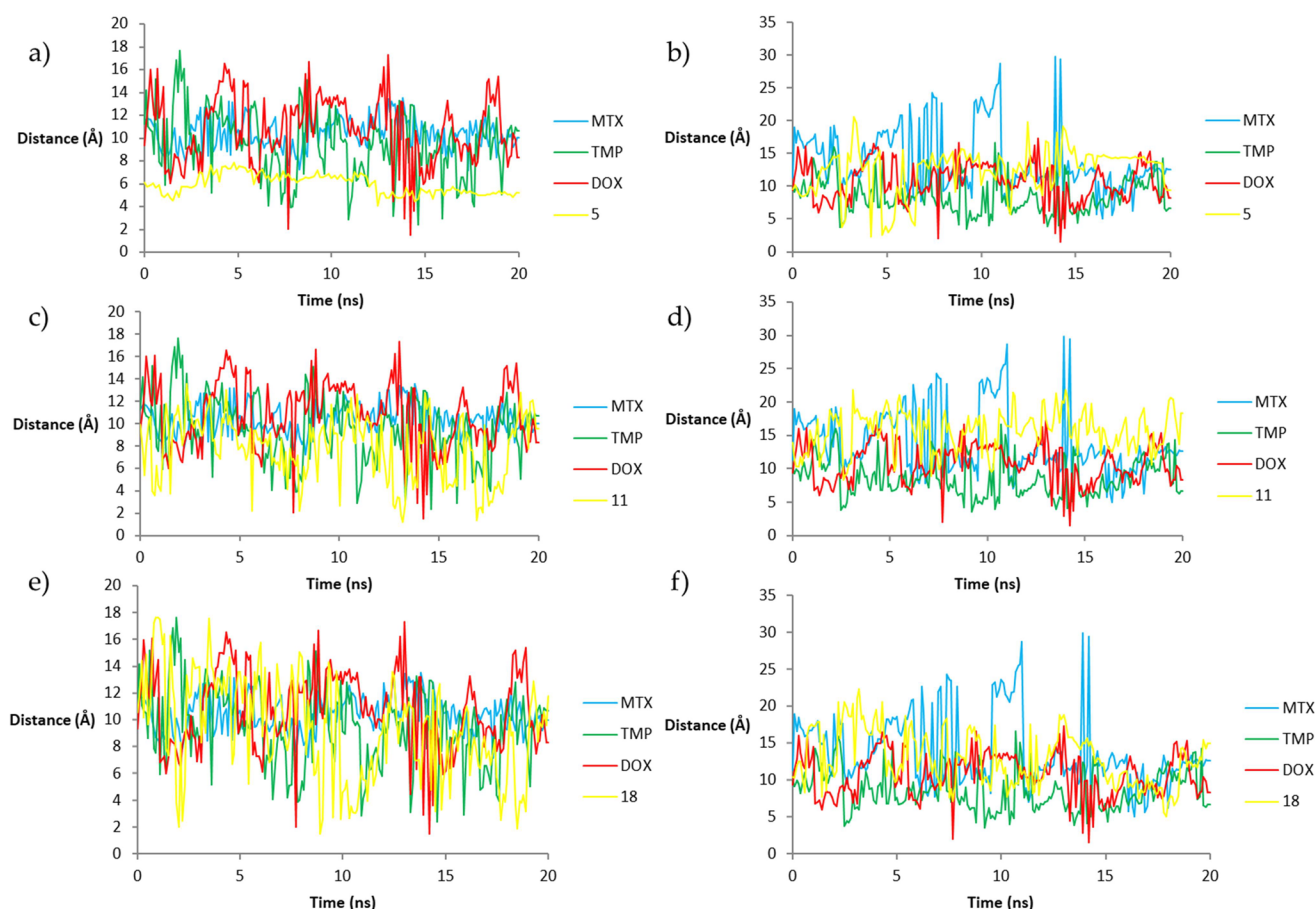


Figure 9. Dependence of the distance between the centres of masses of the ligand and the amino acid with which it most often formed hydrogen bonds on simulation time for ligands: (a) **5**, (c) **11** and (e) **18**, and analogous plots of the distance from the Glu30 residuum for (b) **5**, (d) **11**, (f) **18**.

Table 8. *In vitro* inhibitory activities (IC_{50} , $\mu\text{g/ml}$)^a against breast MCF-7 cancer cell line, human normal skin fibroblasts (HSF) and selectivity indices (SI)^b.

Compounds	MCF-7 IC_{50} ($\mu\text{g/ml}$)	Normal HSF IC_{50} ($\mu\text{g/ml}$)	Selectivity index (SI)
5	2.72	32.56	11.97
11	12.51	84.37	6.74
MTX	56.94	125.62	2.20

^a IC_{50} values indicate an average of duplicate independent experiments.

^bSI: selectivity index calculated by dividing value of IC_{50} against normal cells by IC_{50} against cancer cells. SI < 1: low selectivity, SI (1–3): moderate selectivity, SI > 3: high selectivity.

In vitro anti-proliferative and cytotoxicity assays for derivatives **5** and **11**

Recent evidence has stated that *h*DHFR inhibition may be a promising therapeutic strategy for breast cancer^{47,48}. The most promising compounds **5** and **11** alongside **MTX** as a standard reference were thus evaluated for their anti-proliferative activity against MCF-7 breast cancer cell line known to highly express *h*DHFR using MTT assay⁴⁹. Results were expressed in the form of IC_{50} values, which is the concentration causing 50% cell viability inhibition. Also, cytotoxicity against normal human skin fibroblast was also assessed and selectivity indices (SI) were calculated in order to check their safety profiles (Table 8). Both compounds **5** and **11** demonstrated remarkable potency against MCF-7 with IC_{50} values of 2.72 and 12.51 $\mu\text{g/ml}$, respectively. Compound **5**, exclusively, was found to be nearly 21 fold more potent than **MTX**, while compound **11** was 4.5 times more active than **MTX**. Interestingly, our

tested compounds showed weak cytotoxicity against normal skin fibroblast cells with respective high IC_{50} values of 32.56 and 84.37 $\mu\text{g/ml}$. Compounds **5** and **11** exhibited higher selectivity towards cancer cells over normal cells more than **MTX** with SI 11.97 and 6.74, respectively, implying good safety profile.

Apoptosis induction potential for derivatives 5 and 11

In order to quantitatively determine the apoptotic effects of compounds **5** and **11** in MCF-7 cells, flow cytometric analysis was performed using double staining with Annexin V-FITC/propidium iodide (AV/PI). This assay allows the differentiation between four cell populations: unstained viable cells, PI-stained necrotic cells, FITC-labelled Annexin V-stained early apoptotic cells and both Annexin V and PI-stained late apoptotic cells. Compared to control cells, the percentage of total apoptosis in MCF-7 cells exhibited by compounds **5** and **11** raised from 4.2 to 29.63 and 23.99, respectively, while the percentage of necrosis decreased from 5.13 in control cells and 6.50 in **MTX**-treated cells to be 3.09 and 4.81 thus not showing any significant necrotic hazards on normal body cells (Figure 10). These results might suggest that a probable mechanism of cell growth inhibitory effects of **5** and **11** is *via* induction of apoptosis analogous to **MTX**.

Wound healing assay

In light of the cell apoptosis results for **5** and **11**, it is probable that both compounds may affect cell migration in MCF-7 cells. Thus in order to assess the anti-migratory effects of **5** and **11**, a wound

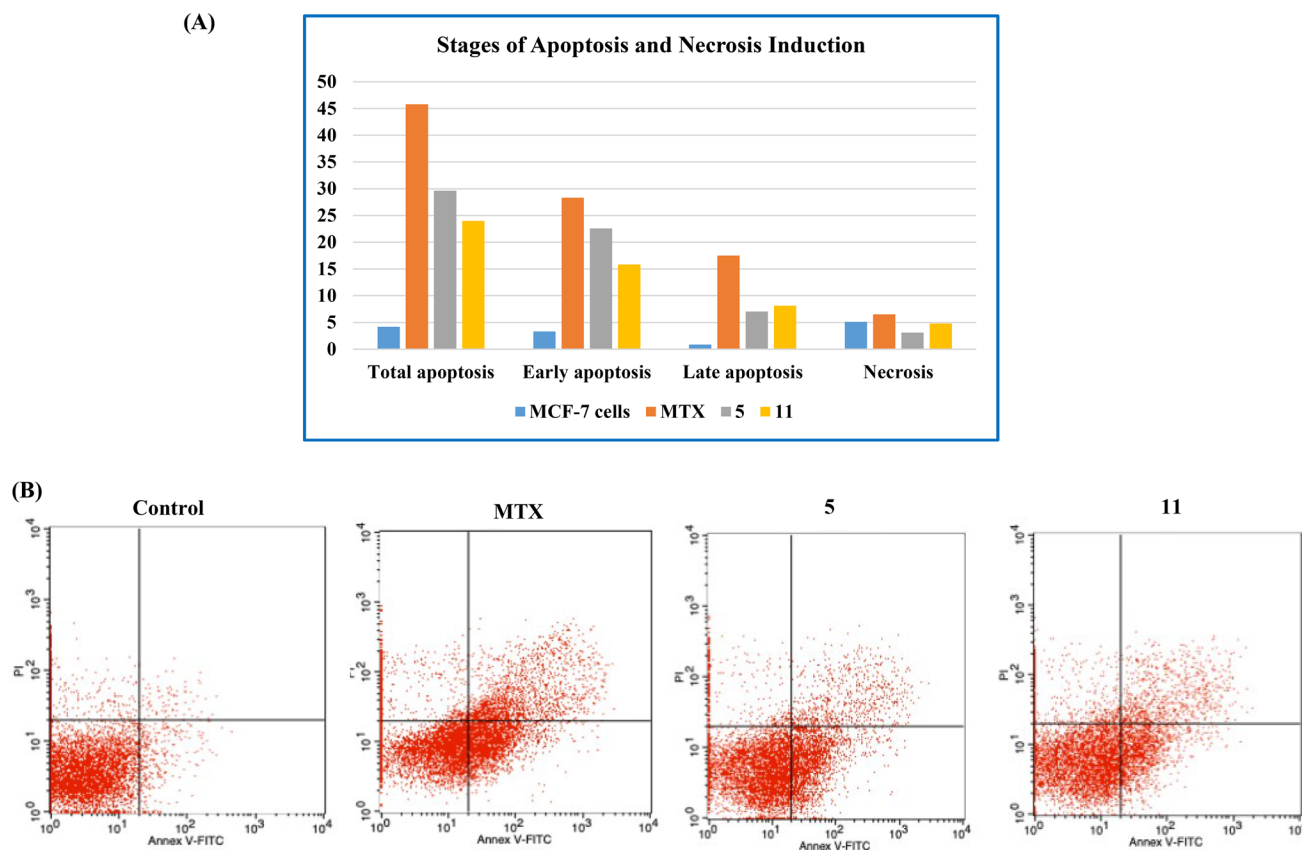


Figure 10. (A) Graphical representation of the stages of cell apoptosis induction and necrosis for compounds **5** and **11** compared to control untreated MCF-7 cells and **MTX**-treated cells, (B) Cell apoptosis dot plots of control MCF-7, **MTX**-treated MCF-7, and compounds **5**- and **11**-treated MCF-7 cells, respectively.

healing assay was conducted (Figure 11). Compounds **5** and **11** were found to induce a significant decrease in the percentage of wound closure following 24h treatment in MCF-7 cells in reference to untreated control cells comparable to **MTX** (Table 9).

In silico drug-likeness and ADMET prediction for 5 and 11

Undesirable physicochemical, pharmacokinetic, and toxicity parameters are main contributors to drug development failures as potential drugs⁵⁰. *In silico* drug-likeness and ADMET prediction were performed to the two promising compounds **5** and **11**, which proved their potent dual activity as DNA minor groove binders and DHFR inhibitors. Employing ADMETlab 3.0 (<https://admetlab3.scbdd.com/>) and PreADME/Tox (<https://preadmet.qsarhub.com/>) online servers, all necessary parameters were computed (Table 10). It was clear that both compounds adhered well to drug-likeness rules with no violation to Lipinski's rule of five⁵¹. In brief, they had molecular weights (Mwt) < 500 Dalton, number of hydrogen bond donors (nHBD) < 5, number of hydrogen bond acceptors (nHBA) < 10 and logarithm of *n*-octanol/water distribution coefficient (logP) < 5. Besides, they showed total polar surface area (TPSA) < 140 Å² facilitating their full intestinal absorption⁵². Additionally, both compounds displayed no violation to Golden triangle rule, thus might have more favourable ADMET profiles⁵³. As predicted, both compounds have respective moderate permeability and high gastrointestinal absorption⁵³ reflected by their computed CaCo-2 and % human intestinal absorption (HIA) values. Notably, they are expected to be permeability glycoprotein (Pgp) inhibitors indicating possibility of uniform distribution and metabolism inside the cancer cell without being effluxed outside⁵⁴. Although pharmacodynamically

they might possess low therapeutic index as viewed from their high % plasma protein binding (PPB > 90%), in contrast, they are expected to manifest moderate CNS side effects due to their low blood-brain barrier (BBB) penetration (moderate BBB range 0.1–2 nm/s). Metabolic profile predictions are also important to expect detoxification of drugs by cytochrome P456 (CYP450)⁵⁵. Both **5** and **11** are predicted to be efficiently metabolised as they are non-inhibitors to different CY450 enzymes. Human liver microsomal (HLM) stability is considered the most utilised parameter that assesses clearance of chemicals by the human liver. Both compounds were assumed to be of excellent stability. Moreover, they showed predicted low values of plasma clearance ($CL_{\text{plasma}} < 5 \text{ ml/min/kg}$) expressing precaution with administration and dose adjustment in order to maintain an average steady-state plasma concentration. In this context, both compounds have intermediate short half-life ($t_{1/2}$: 1–4 h) thus might require careful frequent dosing. Predicting the *in silico* toxicity profiles of both **5** and **11** revealed non-carcinogenicity in rats. However, they might demonstrate moderate cardiac toxicities due to their moderate human-ether-a-go-go gene (*hERG*) inhibition. These overall predicted favourable physicochemical and pharmacokinetic attributes make them strong drug candidates for further optimisation and development.

Conclusion

In conclusion, a series of 14 new arylidene-hydrazinyl-1,3-thiazoles (**5–18**) were designed, synthesised, and biologically evaluated as dual DNA binders and *h*DHFR inhibitors. Based on the biological results, the percentage of decrease in fluorescence of EtBr–DNA

Control MCF-7 cells

5

11

MTX

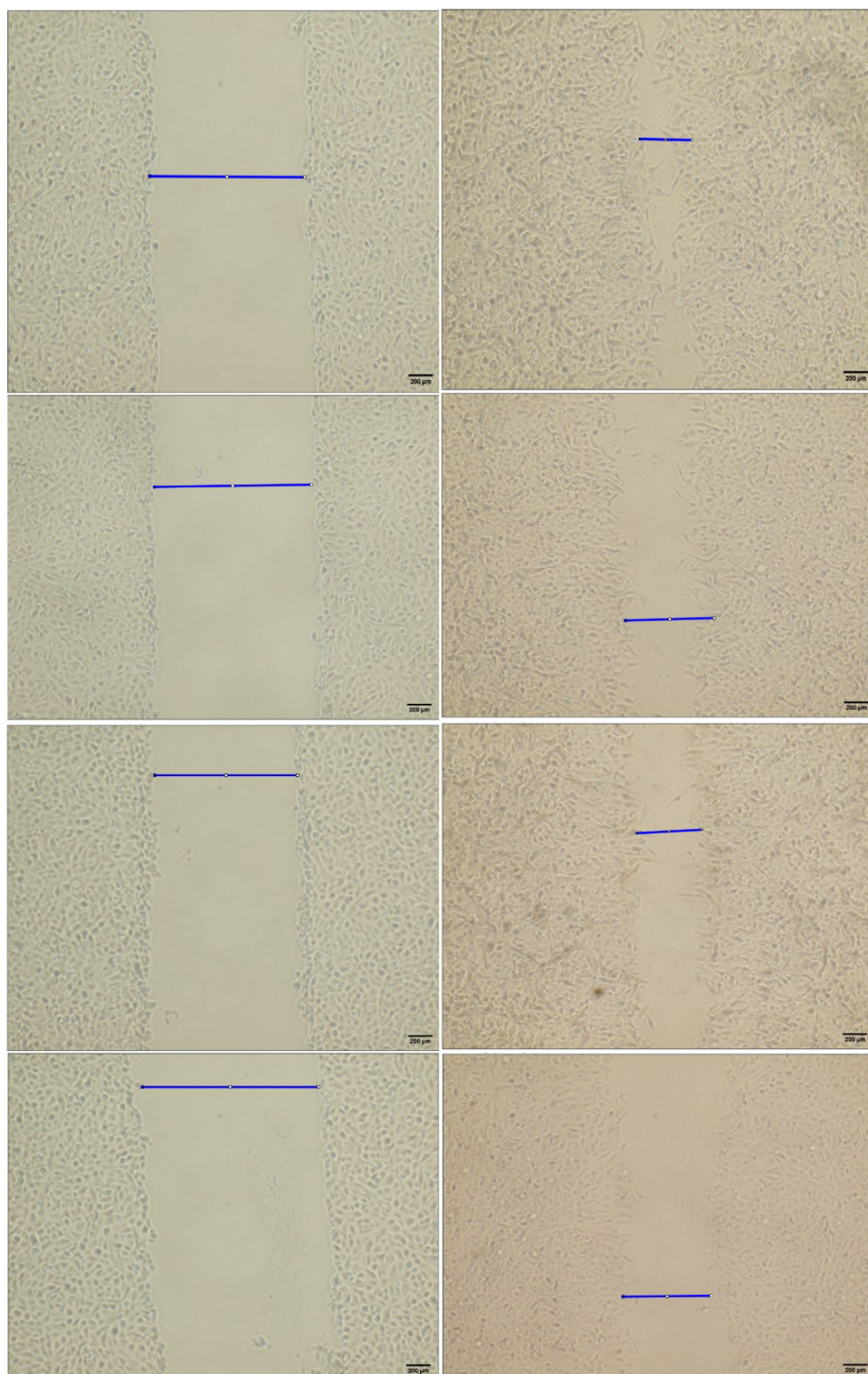


Figure 11. MCF-7 cultured cells treated with compounds **5** and **11** in reference to **MTX** at their IC_{50} concentrations and to control untreated cells at 0 and 24 h. An inverted microscope (Olympus, Japan) at a magnification of $\times 100$ was used to image the wounded cells. The wound edges are joined by a blue line.

complexes by the target compounds revealed that they could bind to the studied DNAs. The data indicated that compounds **5–18** interacted with AT as well as GC-base pairs. The greatest preference was observed for GC-bases pairs to the tested

compounds, besides derivatives **9**, **14**, and **18** which showed preference to AT-base pairs. All target compounds showed high values of T4 coliphage DNA binding confirming their minor groove selectivity. As for *h*DHFR inhibitory activity, only

Table 9. Wound closure percentage in MCF-7 cancer cells in presence of compounds **5** and **11** compared to control untreated and **MTX**-treated cells.

Entry	% Wound closure after 24 h treatment
Control MCF-7	69.94
5	45.19
11	52.72
MTX	45.46

Table 10. Drug-likeness and pharmacokinetic parameters analysed for **5** and **11** using ADMETlab 3.0 and PreADME/Tox online servers.

Parameters	5	11
<i>Drug-likeness</i>		
Mwt	383.05	428.03
nHBD	2	2
nHBA	5	8
logP	4.87	4.82
TPSA	74.58	117.72
<i>Pharmacokinetics</i>		
<i>Absorption</i>		
CaCo-2	18.61	6.35
HIA	97.33	94.65
Pgp	inhibitor	inhibitor
<i>Distribution</i>		
PPB	92.27	92.96
BBB	0.43	0.65
<i>Metabolism</i>		
CYP2C19/CYP2D6/ CYP3A4/	Non-inhibitor	Non-inhibitor
HLM stability	Stable	Stable
<i>Excretion</i>		
CL _{plasma} (ml/min/kg)	2.03	1.76
t _{1/2} (h)	1.09	1.14
<i>Toxicity</i>		
Carcinogenicity in rats	Non-carcinogen	Non-carcinogen
hERG inhibition	Medium risk	Medium risk

compounds **5** and **11** exhibited comparable inhibition to **MTX** and more potent than **TMP**. On the other hand, computational analyses predicted the possible mode of binding of the most active derivatives **5** and **11** in reference to **DOX**, **MTX**, and **TMP**. Despite forming fewer hydrogen bonds than reference ligands, both **5** and **11** demonstrated a stabilising effect on hDHFR as revealed from molecular dynamics results. Anti-breast cancer evaluation confirmed the potent activity of **5** and **11** against MCF-7 cells with least toxicity on normal skin fibroblasts compared to **MTX**. Furthermore, apoptosis and wound healing assays performed for **5** and **11** on MCF-7 revealed the possible mechanism of their antitumor activity. Computed pharmacokinetic and ADMET parameters favoured the potential drug-like properties of **5** and **11** with the possibility of future optimisation towards efficiently breast-targeted cancer therapeutics.

Experimental section

General synthetic materials and methods

Thin-layer chromatography (TLC) on pre-coated aluminium silica gel sheets (60-GF254, Merck, Kenilworth, NJ) was used to follow up the reactions and check homogeneity of the compounds. The ratio of the eluent solvents used was volume to volume. Product spots were visualised using either UV-lamp at λ 254 nm for few seconds or after being exposed to iodine vapour. Melting points were assigned using SMP10-Barloworld Scientific melting point device and were uncorrected. Fourier transform IR (FT-IR) was performed on KBr discs. ¹H NMR and ¹³C NMR spectra were scanned on Joel JNM ECA 500 II spectrometer (500 MHz, 11.75 Tesla) or Bruker high performance digital FT-NMR spectrometer advance III

(400 MHz) using deuterated dimethyl sulfoxide (DMSO-*d*₆) as solvent. Tetramethylsilane (TMS) was used as internal standard and data were reported as δ values (ppm). Signals were designated as: s=singlet, br. s=broad singlet, d=doublet, and m=multiplet. High Resolution Mass Spectra (HRMS) were recorded on a Bruker microOTOF-QIII (Bruker Corporation, Billerica, MA) equipped with electrospray ionisation mode and a time of flight detector (TOF). Elemental analyses were computed on FLASH 2000 CHNS/O analyser, Thermo Scientific GCMS model (ISQ) and results were within \pm 0.4 of the theoretical values.

General procedure for synthesis of the starting compounds (1) and (2)

To an ice-cooled stirred solution of the appropriate benzaldehyde derivative (27 mmol) in ethanol (20 ml) and sodium pyruvate (3 g, 27 mmol) in water (5 ml), an aqueous solution of sodium hydroxide 30% (4 ml) was added dropwisly. Stirring was continued for 2 h at room temperature during which the product separated out and the mixture was then refrigerated overnight. The obtained yellow sodium salt was filtered, washed with ethanol, and left to dry. To a stirred solution of 2N HCl (20 ml), a solution of the proper sodium salt in water (20 ml) was added and stirring was maintained for 1 h in an ice bath. The liberated yellow acids were filtered, air dried, and used as such without further purification.

(E)-4-(4-Chlorophenyl)-2-oxobut-3-enoic acid (1)³⁴. Yellow solid. Yield: 90%, m.p. 139–140°C.

(E)-4-(2,6-dichlorophenyl)-2-oxobut-3-enoic acid (2)³⁷. Pale yellow powder. Yield: 91%, m.p. 153–155°C.

General procedure for synthesis of compounds (3) and (4)

A solution of the appropriate 2-oxobut-3-enoic acid derivative **1** or **2** (4.1 mmol) in ethanol/acetic acid mixture (19:1, 20 ml) and thiosemicarbazide (0.37 g, 4.1 mmol) in water (10 ml) was heated under reflux for 20 min. The obtained solution was poured into icy water and the formed precipitate was filtered, washed with water, air dried, and crystallised from acetic acid.

(2Z,3E)-2-(2-carbamothioylhydrazinylidene)-4-(4-chlorophenyl)but-3-enoic acid (3)³⁴. Yellow solid. Yield: 86%, m.p. 194–196°C.

(2Z,3E)-2-(2-carbamothioylhydrazinylidene)-4-(2,6-dichlorophenyl)but-3-enoic acid (4). Yellow solid. Yield: 78%, m.p. 205–208°C. IR (KBr, ν cm⁻¹): 3500–3000 (broad, OH), 3424, 3300 (NH₂), 3272 (NH), 3177, 3088 (CH-aromatic), 1682 (C=O), 1604 (C=N), 1554, 1535, 1464 (δ NH, C=C), 1391, 1219, 963 (N-C=S). ¹H NMR (500 MHz, DMSO-*d*₆) δ ppm: 6.93, 7.31 (2d, each 1H, *J*=15 Hz, 2 ethenyl C-H), 7.33–7.55 (m, 5H, Ar-H and NH₂), 11.36 (s, 1H, NH), 12.31 (s, 1H, COOH). ¹³C NMR (125 MHz, DMSO-*d*₆) δ ppm: 123.68, 126.94, 128.87, 128.99, 133.30, 133.47, 135.36, 135.57, 139.11, 163.66, 178.44. Anal. Calcd. (%) for C₁₁H₉Cl₂N₃O₂S (318.17) C, 41.52; H, 2.85; N, 13.21; S, 10.08. Found: C, 41.51; H, 3.04; N, 13.49; S, 10.14.

General procedure for synthesis of the target compounds (5–18)

To a solution of the selected thiosemicarbazones **3** or **4** (0.6 mmol) in absolute ethanol (5 ml), the appropriate phenacyl bromide derivative (0.6 mmol) was added. The reaction mixture was heated under reflux for 3 h. The obtained precipitates were filtered, washed with ethanol, air dried, and crystallised from *n*-hexane.

(2Z,3E)-4-(4-Chlorophenyl)-2-(2-(4-phenylthiazol-2-yl)hydrazinylidene)but-3-enoic acid (5). Pale yellow powder. Yield: 51%, m.p. 263–265°C. IR (KBr, ν cm⁻¹): 3400–3000 (broad, OH), 3128 (NH), 3046 (CH-aromatic), 1714 (C=O), 1633 (C=N), 1604, 1538, 1487 (δ NH, C=C), 1237, 1049 (C-S-C). ¹H NMR (500 MHz, DMSO-d₆) δ ppm: 7.03, 7.13 (2d, each 1H, J =16.25 Hz, 2 ethenyl C-H), 7.31–7.85 (m, 10H, Ar-H and thiazole C₅-H), 13.10 (br.s, 1H, COOH). ¹³C NMR (125 MHz, DMSO-d₆) δ ppm: 105.04, 123.85, 125.66 (2C), 128.14, 128.68 (2C), 128.83 (2C), 128.94 (2C), 130.61, 132.77, 135.34, 137.09, 150.21, 160.59, 164.81, 168.34. HRMS (ESI) m/z calcd for C₁₉H₁₄ClN₃O₂S [M+H]⁺ 384.0568, found 384.0522. Anal. Calcd. (%) for C₁₉H₁₄ClN₃O₂S: C, 59.45; H, 3.68; N, 10.95; S, 8.35. Found: C, 59.72; H, 3.82; N, 11.21; S, 8.42.

(2Z,3E)-4-(4-Chlorophenyl)-2-(2-(4-(4-tolyl)thiazol-2-yl)hydrazinylidene)but-3-enoic acid (6). Yellow powder. Yield: 50%, m.p. 245–247°C. IR (KBr, ν cm⁻¹): 3400–3000 (broad, OH), 3130 (NH), 3025 (CH-aromatic), 2917 (CH-aliphatic), 1714 (C=O), 1626 (C=N), 1586, 1514, 1490 (δ NH, C=C), 1296, 1054 (C-S-C). ¹H NMR (500 MHz, DMSO-d₆) δ ppm: 2.31 (s, 3H, CH₃), 7.03, 7.12 (2d, each 1H, J =16.25 Hz, 2 ethenyl C-H), 7.21–7.74 (m, 9H, Ar-H and thiazole C₅-H), 13.02 (br. s, 1H, COOH). ¹³C NMR (125 MHz, DMSO-d₆) δ ppm: 20.86, 105.01, 123.77, 125.54 (2C), 128.62 (2C), 128.86 (2C), 129.31 (2C), 130.06, 132.70, 133.32, 135.28, 137.74, 138.94, 152.37, 164.79, 168.42. HRMS (ESI) m/z calcd for C₂₀H₁₆ClN₃O₂S [M+H]⁺ 398.0724, found 398.0677. Anal. Calcd. (%) for C₂₀H₁₆ClN₃O₂S: C, 60.38; H, 4.05; N, 10.56; S, 8.06. Found: C, 60.59; H, 4.23; N, 10.82; S, 8.17.

(2Z,3E)-4-(4-Chlorophenyl)-2-(2-(4-(4-methoxyphenyl)thiazol-2-yl)hydrazinylidene)but-3-enoic acid (7). Yellow powder. Yield: 68%, m.p. 203–205°C. IR (KBr, ν cm⁻¹): 3400–3000 (broad, OH), 3118 (NH), 3042, 3014 (CH-aromatic), 2928, 2834 (CH-aliphatic), 1727 (C=O), 1614 (C=N), 1591, 1509, 1442 (δ NH, C=C), 1296, 1093 (C-O-C), 1254, 1021 (C-S-C). ¹H NMR (500 MHz, DMSO-d₆) δ ppm: 3.77 (s, 3H, OCH₃), 7.03, 7.11 (2d, each 1H, J = 16 Hz, 2 ethenyl C-H), 6.96–7.81 (m, 9H, Ar-H and thiazole C₅-H). ¹³C NMR (125 MHz, DMSO-d₆) δ ppm: 55.19, 103.47, 114.07 (2C), 126.91, 126.99, 128.58, 128.79, 128.83, 129.28, 130.00, 132.52, 132.69, 133.51, 135.26, 135.46, 136.73, 158.93, 164.71, 168.51. HRMS (ESI) m/z calcd for C₂₀H₁₆ClN₃O₃S [M+H]⁺ 414.0674, found 414.0626. Anal. Calcd. (%) for C₂₀H₁₆ClN₃O₃S: C, 58.04; H, 3.90; N, 10.15; S, 7.75. Found: C, 58.27; H, 4.15; N, 10.37; S, 7.83.

(2Z,3E)-4-(4-Chlorophenyl)-2-(2-(4-(4-fluorophenyl)thiazol-2-yl)hydrazinylidene)but-3-enoic acid (8). Pale yellow powder. Yield: 70%, m.p. 257–259°C. IR (KBr, ν cm⁻¹): 3400–3000 (broad, OH), 3122 (NH), 3074, 3044 (CH-aromatic), 1714 (C=O), 1636 (C=N), 1598, 1508, 1489 (δ NH, C=C), 1300, 1039 (C-S-C). ¹H NMR (500 MHz, DMSO-d₆) δ ppm: 7.03, 7.13 (2d, each 1H, J =16.25 Hz, 2 ethenyl C-H), 7.23–7.91 (m, 9H, Ar-H and thiazole C₅-H), 13.01 (br. s, 1H, COOH). ¹³C NMR (125 MHz, DMSO-d₆) δ ppm: 105.03, 115.59 (2C), 123.68, 127.72 (2C), 128.61 (2C), 128.84 (2C), 130.56, 132.71, 135.25, 135.38, 150.30, 160.87, 162.83, 164.67, 167.91. HRMS (ESI) m/z calcd for C₁₉H₁₃ClFN₃O₂S [M+H]⁺ 402.0474, found 402.0445. Anal. Calcd. (%) for C₁₉H₁₃ClFN₃O₂S: C, 56.79; H, 3.26; N, 10.46; S, 7.98. Found: C, 57.05; H, 3.40; N, 10.78; S, 8.15.

(2Z,3E)-4-(4-Chlorophenyl)-2-(2-(4-(4-chlorophenyl)thiazol-2-yl)hydrazinylidene)but-3-enoic acid (9). White powder. Yield: 69%, m.p. 234–36°C. IR (KBr, ν cm⁻¹): 3400–3000 (broad, OH), 3120

(NH), 3056, 3014 (CH-aromatic), 1725 (C=O), 1632 (C=N), 1578, 1487 (δ NH, C=C), 1321, 1043 (C-S-C). ¹H NMR (500 MHz, DMSO-d₆) δ ppm: 7.02, 7.13 (2d, each 1H, J =16.25 Hz, 2 ethenyl C-H), 7.40–7.88 (m, 9H, Ar-H and thiazole C₅-H), 12.91 (br. s, 1H, COOH). ¹³C NMR (125 MHz, DMSO-d₆) δ ppm: 105.02, 123.63, 127.35 (2C), 128.63 (2C), 128.74 (2C), 128.85 (2C), 130.61, 132.40, 132.73, 132.80, 135.23, 150.24, 162.89, 164.63, 167.40. HRMS (ESI) m/z calcd for C₁₉H₁₃Cl₂N₃O₂S [M+H]⁺ 418.0178, found 418.0136. Anal. Calcd. (%) for C₁₉H₁₃Cl₂N₃O₂S: C, 54.56; H, 3.13; N, 10.05; S, 7.66. Found: C, 54.80; H, 3.37; N, 10.28; S, 7.59.

(2Z,3E)-4-(4-Chlorophenyl)-2-(2-(4-(4-bromophenyl)thiazol-2-yl)hydrazinylidene)but-3-enoic acid (10). White powder. Yield: 51%, m.p. 253–255°C. IR (KBr, ν cm⁻¹): 3400–3000 (broad, OH), 3127 (NH), 3014 (CH-aromatic), 1714 (C=O), 1632 (C=N), 1578, 1487 (δ NH, C=C), 1321, 1042 (C-S-C). ¹H NMR (500 MHz, DMSO-d₆) δ ppm: 7.02, 7.14 (2d, each 1H, J =16.25 Hz, 2 ethenyl C-H), 7.40–7.82 (m, 9H, Ar-H, and thiazole C₅-H), 13.01 (br.s, 1H, COOH). ¹³C NMR (125 MHz, DMSO-d₆) δ ppm: 105.02, 121.02, 123.69, 127.64 (2C), 128.62 (2C), 128.84 (2C), 130.58, 131.64 (2C), 132.70, 133.41, 135.24, 150.22, 162.79, 164.63, 167.48. HRMS (ESI) m/z calcd for C₁₉H₁₃BrClN₃O₂S [M+H]⁺ 461.9740, found 461.9620. Anal. Calcd. (%) for C₁₉H₁₃BrClN₃O₂S: C, 49.31; H, 2.83; N, 9.08; S, 6.93. Found: C, 49.18; H, 3.08; N, 9.32; S, 7.05.

(2Z,3E)-4-(4-Chlorophenyl)-2-(2-(4-(4-nitrophenyl)thiazol-2-yl)hydrazinylidene)but-3-enoic acid (11). Orange powder. Yield: 73%, m.p. 244–246°C. IR (KBr, ν cm⁻¹): 3400–3000 (broad, OH), 3121 (NH), 3070, 3028 (CH-aromatic), 1714 (C=O), 1632 (C=N), 1598, 1516, 1487 (δ NH, C=C), 1548, 1340 (NO₂), 1343, 1047 (C-S-C). ¹H NMR (500 MHz, DMSO-d₆) δ ppm: 6.99, 7.14 (2d, each 1H, J =16.25 Hz, 2 ethenyl C-H), 7.39–8.26 (m, 9H, Ar-H and thiazole C₅-H), 12.78 (br. s, 1H, COOH). ¹³C NMR (125 MHz, DMSO-d₆) δ ppm: 110.56, 124.21 (2C), 126.45 (2C), 128.78 (2C), 129.38 (2C), 132.80, 133.66, 135.24, 136.46, 136.46, 137.23, 146.44, 164.49, 165.06, 168.90. HRMS (ESI) m/z calcd for C₁₉H₁₃ClN₄O₄S [M+H]⁺ 429.0419, found 429.0366. Anal. Calcd. (%) for C₁₉H₁₃ClN₄O₄S: C, 53.21; H, 3.06; N, 13.06; S, 7.48. Found: C, 53.48; H, 3.20; N, 13.33; S, 7.61.

(2Z,3E)-4-(2,6-dichlorophenyl)-2-(2-(4-phenylthiazol-2-yl)hydrazinylidene)but-3-enoic acid (12). Yellow powder. Yield: 50%, m.p. 210–212°C. IR (KBr, ν cm⁻¹): 3400–3000 (broad, OH), 3130 (NH), 3057 (CH-aromatic), 1686 (C=O), 1603 (C=N), 1551, 1528, 1485 (δ NH, C=C), 1286, 1060 (C-S-C). ¹H NMR (500 MHz, DMSO-d₆) δ ppm: 7.10 (d, 1H, J =16.8 Hz, ethenyl C-H), 7.29–7.88 (m, 10H, Ar-H, ethenyl C-H and thiazole C₅-H). ¹³C NMR (125 MHz, DMSO-d₆) δ ppm: 105.01, 124.72, 125.63 (2C), 128.07, 128.75 (2C), 129.21 (2C), 129.66, 130.81, 132.97, 133.59 (2C), 134.23, 140.02, 150.04, 164.45, 167.21. HRMS (ESI) m/z calcd for C₁₉H₁₃Cl₂N₃O₂S [M+H]⁺ 418.0178, found 418.0130. Anal. Calcd. (%) for C₁₉H₁₃Cl₂N₃O₂S: C, 54.56; H, 3.13; N, 10.05; S, 7.66. Found: C, 54.82; H, 3.25; N, 10.34; S, 7.94.

(2Z,3E)-4-(2,6-dichlorophenyl)-2-(2-(4-(4-tolyl)thiazol-2-yl)hydrazinylidene)but-3-enoic acid (13). Yellow powder. Yield: 38%, m.p. 212–214°C. IR (KBr, ν cm⁻¹): 3400–3000 (broad, OH), 3133 (NH), 3031 (CH-aromatic), 2915 (CH-aliphatic), 1698 (C=O), 1617 (C=N), 1584, 1554, 1512 (δ NH, C=C), 1291, 1045 (C-S-C). ¹H NMR (500 MHz, DMSO-d₆) δ ppm: 2.31 (s, 3H, CH₃), 7.08 (d, 1H, J =17 Hz, ethenyl C-H), 7.21–7.75 (m, 9H, Ar-H, ethenyl C-H and thiazole C₅-H), 13.12 (br. s, 1H, COOH). ¹³C NMR (125 MHz, DMSO-d₆) δ ppm: 20.86, 105.03, 124.69, 125.56 (2C), 129.20 (2C), 129.30 (2C), 129.62,

130.68, 132.94, 133.60 (2C), 135.63, 137.46, 142.44, 150.19, 164.47, 167.68. HRMS (ESI) m/z calcd for $C_{20}H_{15}Cl_2N_3O_2S$ $[M+H]^+$ 432.0335, found 432.0304. Anal. Calcd. (%) for $C_{20}H_{15}Cl_2N_3O_2S$: C, 55.56; H, 3.50; N, 9.72; S, 7.42. Found: C, 55.35; H, 3.71; N, 9.98; S, 7.51.

(2Z,3E)-4-(2,6-dichlorophenyl)-2-(2-(4-(4-methoxyphenyl)thiazol-2-yl)hydrazinylidene)but-3-enoic acid (14). Yellow powder. Yield: 30%, m.p. 221–223 °C. IR (KBr, ν cm^{-1}): 3400–3000 (broad, OH), 3120 (NH), 3073, 3001 (CH-aromatic), 2934, 2835 (CH-aliphatic), 1702 (C=O), 1617 (C=N), 1582, 1551, 1510, 1463 (δ NH, C=C), 1296, 1114 (C-O-C), 1255, 1029 (C-S-C). 1H NMR (500 MHz, DMSO- d_6) δ ppm: 3.86 (s, 3H, OCH_3), 6.96 (d, 2H, $J=8.5$ Hz, methoxyphenyl $C_{2,6}$ -H), 7.08 (d, 1H, $J=17$ Hz, ethenyl C-H), 7.24–7.78 (m, 7H, Ar-H, ethenyl C-H and thiazole C_5 -H), 13.00 (br. s, 1H, COOH). ^{13}C NMR (125 MHz, DMSO- d_6) δ ppm: 55.19, 105.04, 114.09 (2C), 124.70, 127.01 (2C), 129.21 (2C), 129.66, 130.72, 132.92 (2C), 133.58, 134.02, 138.91, 151.23, 159.18, 164.45, 167.69. HRMS (ESI) m/z calcd for $C_{20}H_{15}Cl_2N_3O_3S$ $[M+H]^+$ 448.0284, found 448.0243. Anal. Calcd. (%) for $C_{20}H_{15}Cl_2N_3O_3S$: C, 53.58; H, 3.37; N, 9.37; S, 7.15. Found: C, 53.70; H, 3.49; N, 9.61; S, 7.25.

(2Z,3E)-4-(2,6-dichlorophenyl)-2-(2-(4-(4-fluorophenyl)thiazol-2-yl)hydrazinylidene)but-3-enoic acid (15). Yellow powder. Yield: 57%, m.p. 225–227 °C. IR (KBr, ν cm^{-1}): 3400–3000 (broad, OH), 3171 (NH), 3123, 3076 (CH-aromatic), 1701 (C=O), 1628 (C=N), 1582, 1499, 1431 (δ NH, C=C), 1284, 1055 (C-S-C). 1H NMR (500 MHz, DMSO- d_6) δ ppm: 7.07 (d, 1H, $J=17$ Hz, ethenyl C-H), 7.22–7.91 (m, 9H, Ar-H, ethenyl C-H and thiazole C_5 -H), 13.07 (br. s, 1H, COOH). ^{13}C NMR (125 MHz, DMSO- d_6) δ ppm: 105.02, 115.62 (2C), 124.76, 127.73 (2C), 129.22 (2C), 129.68, 130.65, 132.93, 133.61 (2C), 135.61, 138.89, 150.21, 160.90, 162.85, 164.43. HRMS (ESI) m/z calcd for $C_{19}H_{12}Cl_2FN_3O_2S$ $[M+H]^+$ 436.0084, found 436.0039. Anal. Calcd. (%) for $C_{19}H_{12}Cl_2FN_3O_2S$: C, 52.31; H, 2.77; N, 9.63; S, 7.35. Found: C, 52.49; H, 2.88; N, 9.91; S, 7.52.

(2Z,3E)-4-(2,6-dichlorophenyl)-2-(2-(4-(4-chlorophenyl)thiazol-2-yl)hydrazinylidene)but-3-enoic acid (16). Yellow powder. Yield: 78%, m.p. 226–228 °C. IR (KBr, ν cm^{-1}): 3400–3000 (broad, OH), 3169 (NH), 3119 (CH-aromatic), 1701 (C=O), 1617 (C=N), 1581, 1486, 1430 (δ NH, C=C), 1288, 1055 (C-S-C). 1H NMR (500 MHz, DMSO- d_6) δ ppm: 7.07 (d, 1H, $J=16$ Hz, ethenyl C-H), 7.26–7.89 (m, 9H, Ar-H, ethenyl C-H and thiazole C_5 -H), 13.16 (br. s, 1H, COOH). ^{13}C NMR (125 MHz, DMSO- d_6) δ ppm: 105.01, 124.79, 127.37 (2C), 128.75 (2C), 129.21 (2C), 129.68, 130.64, 132.43, 132.92, 133.60 (2C), 138.91, 141.09, 150.23, 164.37, 167.65. HRMS (ESI) m/z calcd for $C_{19}H_{12}Cl_3N_3O_2S$ $[M+H]^+$ 451.9789, found 451.9734. Anal. Calcd. (%) for $C_{19}H_{12}Cl_3N_3O_2S$: C, 50.40; H, 2.67; N, 9.28; S, 7.07. Found: C, 50.63; H, 2.84; N, 9.54; S, 7.20.

(2Z,3E)-4-(2,6-dichlorophenyl)-2-(2-(4-(4-bromophenyl)thiazol-2-yl)hydrazinylidene)but-3-enoic acid (17). Yellow powder. Yield: 73%, m.p. 228–230 °C. IR (KBr, ν cm^{-1}): 3400–3000 (broad, OH), 3174 (NH), 3118, 3042 (CH-aromatic), 1701 (C=O), 1642 (C=N), 1579, 1554, 1483 (δ NH, C=C), 1286, 1054 (C-S-C). 1H NMR (500 MHz, DMSO- d_6) δ ppm: 7.07 (d, 1H, $J=16.5$ Hz, ethenyl C-H), 7.27–7.83 (m, 9H, Ar-H, ethenyl C-H and thiazole C_5 -H), 13.18 (br. s, 1H, COOH). ^{13}C NMR (125 MHz, DMSO- d_6) δ ppm: 105.02, 121.07, 124.78, 127.68 (2C), 129.22 (2C), 129.70, 130.71, 131.66 (2C), 132.94, 133.59 (2C), 135.63, 147.72, 150.31, 164.38, 167.89. HRMS (ESI) m/z calcd for $C_{19}H_{12}BrCl_2N_3O_2S$ $[M+H]^+$ 498.9284, found 497.9202. Anal. Calcd. (%) for $C_{19}H_{12}BrCl_2N_3O_2S$: C, 45.90; H, 2.43; N, 8.45; S, 6.45. Found: C, 46.18; H, 2.60; N, 8.72; S, 6.39.

(2Z,3E)-4-(2,6-dichlorophenyl)-2-(2-(4-(4-nitrophenyl)thiazol-2-yl)hydrazinylidene)but-3-enoic acid (18). Yellow powder. Yield: 75%, m.p. 240–242 °C. IR (KBr, ν cm^{-1}): 3400–3000 (broad, OH), 3198 (NH), 3122, 3062 (CH-aromatic), 1692 (C=O), 1624 (C=N), 1598, 1513, 1433 (δ NH, C=C), 1557, 1341 (NO_2), 1288, 1054 (C-S-C). 1H NMR (500 MHz, DMSO- d_6) δ ppm: 7.10 (d, 1H, $J=16.8$ Hz, ethenyl C-H), 7.32–8.30 (m, 9H, Ar-H, ethenyl C-H and thiazole C_5 -H). ^{13}C NMR (125 MHz, DMSO- d_6) δ ppm: 111.05, 124.11 (2C), 124.92, 126.51 (2C), 129.18 (2C), 129.66, 130.47, 132.86, 133.61 (2C), 137.83, 139.87, 146.43, 149.32, 164.29, 167.41. HRMS (ESI) m/z calcd for $C_{19}H_{12}Cl_2N_4O_4S$ $[M+H]^+$ 463.0029, found 462.9981. Anal. Calcd. (%) for $C_{19}H_{12}Cl_2N_4O_4S$: C, 49.26; H, 2.61; N, 12.09; S, 6.92. Found: C, 49.37; H, 2.85; N, 12.37; S, 7.08.

The ethidium bromide assay – DNA-binding effects

All reagents were purchased from Fluka (Sigma-Aldrich sp. z o.o., Poznań, Poland). Ethidium bromide was purchased from Carl Roth GmbH (Karlsruhe, Germany). Plasmid pBR322 was purchased from Fermentas Life Science (Vilnius, Lithuania). The activity of the investigated compound **5–18** on DNAs was determined in accordance with a procedure described previously⁵⁶. Each well of 96-well plate was loaded with Tris buffer containing ethidium bromide (0.1 M Tris, 1 M NaCl, pH 8.0, 0.5 mM EtBr final concentration, 100 μ l). Then, 15 μ g DNA (pBR322, calf thymus DNA, T4 coliphage DNA, poly(dA-dT)₂, and poly(dG-dC)₂) as water solution (0.05 μ g/ μ l) and standards or compound **5–18** (1 μ l of a 1 mM solution in water) were added to each well, to obtain a final concentration of 10 μ M. After incubation at 25 °C for 30 min. the fluorescence was recorded on Infinite M200 fluorescence spectrophotometer (TECAN, Männedorf, Switzerland) (ex. 546 nm, em. 595 nm) in duplicate experiments with two control wells (no drug = 100% fluorescence, no DNA = 0% fluorescence).

Dihydrofolate reductase (DHFR) inhibition assay

hDHFR $\geq 80\%$ (SDS-PAGE), recombinant, expressed in *E. coli*, ≥ 1 units/mg protein was purchased from Sigma-Aldrich (catalogue no. D6566). The effects of target derivatives (**5–18**) on the activity of recombinant human DHFR were determined by DHFR inhibition according to the reported methods and according to the instructions supplied with the set and recommended by the producer manufacturer⁵⁷. The changes in absorbance ($\Delta OD/min$) were measured by the spectrophotometer Infinite M200 fluorescence spectrophotometer (TECAN, Männedorf, Switzerland), kinetic program (reading every 15 s for 2.5 min). Results were reported as IC_{50} (50% inhibition of enzymatic activity).

Molecular docking

In this study, two types of docking were carried out. First one, the ligand under study was placed at the location of the reference ligand in the structure from the PDB database. Both the reference ligand and solvent molecules were removed from the protein structure beforehand. This type of docking is further referred to as “fixed-window docking”, which always includes the position of the deleted reference ligand. The analysed area (a cube with a side length of 20 Å) did not change its coordinates, which were: $x_0 = 30$ Å, $y_0 = 16$ Å, $z_0 = 2$ Å for the centre of the cube. The second procedure, referred to as “variable window docking”, involved repeated dockings with the box shifting to capture the full diversity of the target protein structure. This procedure utilised an in-house script. For each box position, docking calculations were performed to generate the best-scored poses (i.e. those with the lowest ΔG values). Consequently, a variety of poses,

potentially differing in placement, were obtained. Here, the analysed area (a cube with a side length of 20 Å) changed its coordinates in the range: x : 24–36 Å every two units; y : 10–22 Å every two units; z : –4–8 Å every two units; the starting coordinates of the centre of the area were the same as for docking with a fixed window: $x_0 = 30$ Å, $y_0 = 16$ Å, $z_0 = 2$ Å. As a result, 343 poses were generated for each of the tested compounds, and those with energies below –9 kcal/mol were selected for statistical analysis. In both cases, the crystal structure of the hDHFR protein, extracted from the PDB database (PDB: 1U72, resolution 1.9 Å, <https://www.rcsb.org/structure/1U72>), was utilised. Reference ligand structures were also downloaded from the PDB database: **MTX** (<https://www.rcsb.org/ligand/MTX>), **TMP** (<https://www.rcsb.org/ligand/TOP>), **DOX** (<https://www.rcsb.org/ligand/DM2>). The prepared model was pre-treated for docking by cleansing its structures of solvent and ions, and by adding polar hydrogen atoms and Kollman charges⁵⁸. AutoDock Vina version 1.2.5 software was used to carry out molecular docking^{59,60}. To improve accuracy, the EXHAUSTIVENESS parameter was set to 100 (default = 8), ensuring optimal performance⁶¹. BIOVIA Discovery Studio Visualizer⁶² was employed to analyse ligand-protein interactions. A re-docking process was conducted to validate the results. The RMSD parameter, gauging the variance in atom distances between compared molecules, was computed yielding a value of 0.428 Å, indicating a satisfactory outcome. PyMol 2.5.5 software⁶³ was employed for RMSD calculation and system categorisation based on positioning. The statistical analysis of molecular docking results was performed using Statistica 13.0 software (StatSoft; Tulsa, OK).

Molecular dynamics

MD simulations were performed using NAMD 2.14⁶⁴ and VMD 1.9.3⁶⁵ utilising force field CHARM22⁶⁶. The ligands after docking were prepared with the CHARMM-GUI (<https://www.charmm-gui.org/>) online environment. The process of preparing the system for simulation included; embedding the system in a solvation shell, ionisation of the system with 0.15 M NaCl to make the conditions similar to the physiological environment and conducting a simulation in which the system was gradually heated from 0 K to 310 K (MINIMIZE – 50000 and EQUALIBRATION – 1 ns). The actual simulations were then carried out, each of which lasted 20 ns, with a duration of 2 fs per step. During the simulations, a constant temperature of 310 K and a constant pressure of one atmosphere were maintained. This was possible due to the use of Langevin dynamics - damping factor equal to 5 (1/ps) and Langevin piston - decay period equal to 100 fs.

In vitro anti-proliferative assay

Breast cancer (MCF-7) cell line was purchased from the American Type Culture Collection (ATCC; Manassas, VA). Human skin fibroblasts (HSF) were cultured at Centre of Excellence for Research in Regenerative Medicine and Application (CERRMA), Faculty of Medicine, Alexandria University. MCF-7 cells were cultivated in Dulbecco's modified Eagle's medium (DMEM) complemented with foetal bovine serum (FBS) 10% (v/v) and antibiotics 0.5% (v/v) (100 U/ml penicillin and 100 U/ml streptomycin). All utilised solvents and reagents were of high purity and used as received. All culture products and media; FBS, DMEM, phosphate-buffered saline (PBS), EDTA trypsin and antibiotics (penicillin/streptomycin) were purchased from Gibco, Carlsbad, CA. 3-(4,5-dimethylthiazol-2-yl)-2,5-diphenyltetrazolium bromide (MTT) was purchased from Sigma-Aldrich (St. Louis, MO). Investigated compounds **5** and **11** were examined on mammary

gland breast cancer (MCF-7) in reference to **MTX**. The half maximal inhibitory concentrations (IC_{50}) which showed the compounds' concentrations that inhibited 50% of cells growth after 24 h incubation with the tested compound using MTT assay, by applying repeated doses of 5–100 µg/ml to cells that were seeded into a 96-well plate. The optical density (OD) of DMSO was measured using a microplate ELISA reader (Infinite F50, TECAN) at wave length of 570 nm.

Normal cytotoxicity evaluation using human skin fibroblasts

For normal cytotoxicity evaluation, normal HSF was prepared according to a previously reported methodology^{67,68}. In brief, cultivated HSF cells were cultivated in 1 ml of 0.1% gelatine added to each well of a 6-well plate. The plate was set aside for 30–60 min. The gelatine solution and 800 µl of added DMEM/20% FBS media to each well was aspirated. Then, the 6-well plate was placed in an incubator at 37 °C and monitored daily to ensure there is a film of media coating the bottom of the well. After one week, amount of media was increased to 2 ml of complete DMEM/20%FBS and changed every 2–3 d. Once fibroblasts were confluent, they were transferred to 3X T175 flasks, freezed in complete DMEM media and 10% DMSO at 1×10^6 cells/ml per vial to afford ready HSF cells. The test compounds were subsequently incubated with HSF cells for 24 h. Cell viability was assayed and IC_{50} concentrations were determined by MTT as described in the anti-proliferative assay.

Apoptosis induction

Effect of compounds **5** and **11** in reference to **MTX** on inducing apoptosis in MCF-7 cells was investigated using Annexin V-FITC/PI co-staining technique where four types of cells are distinguished (early and late apoptotic, necrotic and viable cells). Seeding of 250,000 cells per well into a six-well plate was conducted, and the corresponding IC_{50} of the test compounds and **MTX** were applied to the cells. 24 h incubation period was followed by 30 min of 4 °C UV light, in reference to untreated and unlit negative controls cells. Flow cytometry study was performed employing a flow cytometer (BD, Bioscience, Franklin Lakes, NJ), and results were recorded by BD Bioscience's FACS Diva software.

Wound healing assay

MCF-7 cells were trypsinised and treated in a 6-well plate then smeared on glass slides after fixation with ethanol. An Olympus DP20 digital camera connected to an Olympus BX41 microscope was used for the cytological investigation at $\times 200$ and $\times 400$ powers. The confluent monolayer was created by cultivating cells on 6-well culture plates at seeding density of 25×10^4 /well. Then, the cell monolayer was gently scratched using a sterile 200-µl pipette tip. Scratched wells treated with **MTX** were employed as positive controls then cells were treated with compounds **5** and **11** at their investigated IC_{50} values following a PBS wash. Wound healing was observed and measured at zero and 24 h. The wound was imaged using an inverted microscope (Olympus, Tokyo, Japan) at $\times 100$ magnification. The wound gap's horizontal distance was assessed using Image J (version 1.53 C, NIH, Bethesda, MD) to evaluate the cell migration rate and % wound closure *via* the following equation: %Wound closure = $100 - [(A_t/A_0) \times 100]$, in which A_t represents the wound area at time t and A_0 represents its initial area.

Author contribution

Conception and design: M. El-Wakil, H. A. Abd El-Razik, F. S. G. Soliman, D. Drozdowska; methodology, analysis and interpretation of data: M. El-Wakil, H. El-Dershaby, R. Ghazala, A. Wróbel-Tałałaj, C. Parzych, A. Ratkiewicz, B. Kolesińska; writing –drafting of the paper: M. El-Wakil, R. Ghazala, D. Drozdowska, A. Wróbel-Tałałaj, C. Parzych, A. Ratkiewicz, B. Kolesińska; revision for intellectual content and final approval of the version: M. El-Wakil, H. A. Abd El-Razik, F. S. G. Soliman. Authors agreed to be accountable for all aspects of the work.

Disclosure statement

The authors claim no conflict of interest about this work.

Funding

No funding was received

Data availability statement

The authors confirm that the data supporting the findings of this study are available within the article and its supplemental materials.

References

- [accessed 2024 Apr 15]. <https://www.who.int/news-room/fact-sheets/detail/cancer>.
- [accessed 2024 Apr 15]. <https://www.who.int/news/item/03-02-2023-who-launches-new-roadmap-on-breast-cancer>.
- Anand U, Dey A, Chandel AKS, Sanyal R, Mishra A, Pandey DK, De Falco V, Upadhyay A, Kandimalla R, Chaudhary A, et al. Cancer chemotherapy and beyond: current status, drug candidates, associated risks and progress in targeted therapeutics. *Genes Dis.* 2023;10(4):1367–1401.
- Zafar A, Khan MJ, Abu J, Naeem A. Revolutionizing cancer care strategies: immunotherapy, gene therapy, and molecular targeted therapy. *Mol Biol Rep.* 2024;51(1):219–232.
- Gavande NS, VanderVere-Carozza PS, Hinshaw HD, Jalal SI, Sears CR, Pawelczak KS, Turchi JJ. DNA repair targeted therapy: the past or future of cancer treatment? *Pharmacol Ther.* 2016;160:65–83.
- O'Connor MJ. Targeting the DNA damage response in cancer. *Mol Cell.* 2015;60(4):547–560.
- Amin K, Taha A, George R, Mohamed N, El-Senduny F. Synthesis, antitumor activity evaluation, and DNA-binding study of coumarin-based agents. *Arch Pharm (Weinheim).* 2018;351(1):1700199.
- Guin PS, Das S, Mandal PC. Sodium 1, 4-dihydroxy-9, 10-anthraquinone- 2-sulphonate interacts with calf thymus DNA in a way that mimics anthracycline antibiotics: an electrochemical and spectroscopic study. *J of Physical Organic Chem.* 2010;23(6):477–482.
- Hagner N, Joerger M. Cancer chemotherapy: targeting folic acid synthesis. *Cancer Manag Res.* 2010;2:293–301.
- Kong D, Dolzhenko A. Dihydrofolate reductase inhibitors as anticancer agents: progress and perspectives in drug design and development. *Interdisciplinary cancer research.* Cham: Springer; 2024. p. 1–36.
- Awad HS, Riad KF, Farghaly U. Management of methotrexate toxicity. *J Adv Biomed Pharm Sci.* 2021;4:32–36.
- Wróbel A, Arciszewska K, Maliszewski D, Drozdowska D. Trimethoprim and other nonclassical antifolates an excellent template for searching modifications of dihydrofolate reductase enzyme inhibitors. *J Antibiot (Tokyo).* 2020;73(1):5–27.
- Petrou A, Fesatidou M, Geronikaki A. Thiazole ring—A biologically active scaffold. *Molecules.* 2021;26(11):3166–3240.
- Kassem AF, Althomali RH, Anwar MM, El-Sofany WI. Thiazole moiety: a promising scaffold for anticancer drug discovery. *J Mol Struct.* 2024;1303:137510.
- Aggarwal R, Hooda M, Kumar P, Kumar S, Singh S, Chandra R. An expeditious on-water regioselective synthesis of novel arylidene-hydrazinyl-thiazoles as DNA targeting agents. *Bioorg Chem.* 2023;136:106524.
- El-Wakil MH, El-Yazbi AF, Ashour HMA, Khalil MA, Ismail KA, Labouta IM. Discovery of a novel DNA binding agent via design and synthesis of new thiazole hybrids and fused 1,2,4-triazines as potential antitumor agents: computational, spectrometric and in silico studies. *Bioorg Chem.* 2019;90:103089.
- Alves JEF, de Oliveira JF, de Lima Souza TRC, de Moura RO, de Carvalho Júnior LB, Alves de Lima MdC, de Almeida SMV. Novel indole-thiazole and indole-thiazolidinone derivatives as DNA groove binders. *Int J Biol Macromol.* 2021;170:622–635.
- Santos-Junior PFdS, Nascimento JdS, da Silva ECD, Monteiro KLC, de Freitas JD, de Lima Lins S, Maciel TMS, Cavalcanti BC, V. Neto JdB, de Abreu FC, et al. Synthesis of hybrids thiazole–quinoline, thiazole–indole and their analogs: in vitro anti-proliferative effects on cancer cell lines, DNA binding properties and molecular modeling. *New J Chem.* 2021;45(31):13847–13859.
- Al-Rashood ST, Aboldahab IA, Nagi MN, Abouzeid LA, Abdel-Aziz AAM, Abdel-Hamide SG, Youssef KM, Al-Obaid AM, El-Subbagh HI. Synthesis, dihydrofolate reductase inhibition, antitumor testing, and molecular modeling study of some new 4(3H)-quinazolinone analogs. *Bioorg Med Chem.* 2006;14(24):8608–8621.
- El-Gazzar YI, Georgey HH, El-Messery SM, Ewida HA, Hassan GS, Raafat MM, Ewida MA, El-Subbagh HI. Synthesis, biological evaluation and molecular modeling study of new (1,2,4-triazole or 1,3,4-thiadiazole)-methylthio-derivatives of quinazolin-4(3H)-one as DHFR inhibitors. *Bioorg Chem.* 2017;72:282–292.
- Al-Omary FAM, Hassan GS, El-Messery SM, Nagi MN, Habib E-SE, El-Subbagh HI. Nonclassical antifolates, part 3: synthesis, biological evaluation and molecular modeling study of some new 2-heteroarylthio-quinazolin-4-ones. *Eur J Med Chem.* 2013;63:33–45.
- Ewida MA, Abou El Ella DA, Lasheen DS, Ewida HA, El-Gazzar YI, El-Subbagh HI. Imidazo[2',1':2,3]thiazolo[4,5-d]pyridazinone as a new scaffold of DHFR inhibitors: synthesis, biological evaluation and molecular modeling study. *Bioorg Chem.* 2018;80:11–23.
- Ewida MA, Abou El Ella DA, Lasheen DS, Ewida HA, El-Gazzar YI, El-Subbagh HI. Thiazolo[4,5-d]pyridazine analogues as a new class of dihydrofolate reductase (DHFR) inhibitors: synthesis, biological evaluation and molecular modeling study. *Bioorg Chem.* 2017;74:228–237.
- Al-Omary FAM, Abou-Zeid LA, Nagi MN, Habib E-SE, Abdel-Aziz AA-M, El-Azab AS, Abdel-Hamide SG, Al-Omar MA, Al-Obaid AM, El-Subbagh HI, et al. Non-classical antifolates. Part 2: synthesis, biological evaluation, and molecular modeling study of some new 2,6-substituted-quinazolin-4-ones. *Bioorg Med Chem.* 2010;18(8):2849–2863.

25. Al-Rashood ST, Hassan GS, El-Messery SM, Nagi MN, Habib E-SE, Al-Omary FAM, El-Subbagh HI. Synthesis, biological evaluation and molecular modeling study of 2-(1,3,4-thiadiazolyl-thio and 4-methyl-thiazolyl-thio)-quinazolin-4-ones as a new class of DHFR inhibitors. *Bioorg Med Chem Lett*. 2014;24(18):4557–4567.
26. Moharram EA, El-Sayed SM, Ghabbour HA, El-Subbagh HI. Synthesis, molecular modeling simulations and anticancer activity of some new Imidazo[2,1-b]thiazole analogues as EGFR/HER2 and DHFR inhibitors. *Bioorg Chem*. 2024;150:107538.
27. El-Subbagh HI, Hassan GS, El-Messery SM, Al-Rashood ST, Al-Omary FAM, Abulfadl YS, Shabayek MI. Nonclassical antifolates, part 5. Benzodiazepine analogs as a new class of DHFR inhibitors: synthesis, antitumor testing and molecular modeling study. *Eur J Med Chem*. 2014;74:234–245.
28. Hassan GS, El-Messery SM, Al-Omary FAM, Al-Rashood ST, Shabayek MI, Abulfadl YS, Habib E-SE, El-Hallouty SM, Fayad W, Mohamed KM, et al. Nonclassical antifolates, part 4. 5-(2-Aminothiazol-4-yl)-4-phenyl-4H-1,2,4-triazole-3-thiols as a new class of DHFR inhibitors: synthesis, biological evaluation and molecular modeling study. *Eur J Med Chem*. 2013;66:135–145.
29. Wolter FE, Molinari L, Socher ER, Schneider K, Nicholson G, Beil W, Seitz O, Süssmuth RD. Synthesis and evaluation of a netropsin–proximicin-hybrid library for DNA binding and cytotoxicity. *Bioorg Med Chem Lett*. 2009;19(14):3811–3815.
30. Riyadh S, El-Motairi S, Ahmed H, Khalil K, Habib ES. Synthesis, biological evaluation, and molecular docking of novel thiazoles and [1,3,4]thiadiazoles incorporating sulfonamide group as DHFR inhibitors. *Chem Biodivers*. 2018;15(9):e1800231.
31. El-Wakil MH, Teleb M. Transforming type II to type I c-met kinase inhibitors via combined scaffold hopping and structure-guided synthesis of new series of 1,3,4-thiadiazolo[2,3-c]-1,2,4-triazin-4-one derivatives. *Bioorg Chem*. 2021;116:105304.
32. El-Wakil MH, Meheissen MA, Abu-Serie MM. Nitrofurazone repurposing towards design and synthesis of novel apoptotic-dependent anticancer and antimicrobial agents: Biological evaluation, kinetic studies and molecular modeling. *Bioorg Chem*. 2021;113:104971.
33. El-Wakil MH, Khattab SN, El-Yazbi AF, El-Nikhely N, Soffar A, Khalil HH. New chalcone-tethered 1,3,5-triazines potentiate the anticancer effect of cisplatin against human lung adenocarcinoma A549 cells by enhancing DNA damage and cell apoptosis. *Bioorg Chem*. 2020;105:104393.
34. El-Wakil MH, Ashour HM, Saudi MN, Hassan AM, Labouta IM. Design, synthesis and molecular modeling studies of new series of antitumor 1,2,4-triazines with potential c-Met kinase inhibitory activity. *Bioorg Chem*. 2018;76:154–165.
35. Ashour HM, El-Wakil MH, Khalil MA, Ismail KA, Labouta IM. Synthesis of some (E)-6-[2-(furan-2-yl)ethenyl]-1,2,4-triazin-5-ones and their biological evaluation as antitumor agents. *Med Chem Res*. 2013;22(4):1909–1924.
36. El-Wakil MH, Ashour HM, Saudi MN, Hassan AM, Labouta IM. Target identification, lead optimization and antitumor evaluation of some new 1,2,4-triazines as c-Met kinase inhibitors. *Bioorg Chem*. 2017;73:154–169.
37. El-Wakil MH, El-Dershaby HA, Ghazallah RA, El-Yazbi AF, Abd El-Razik HA, Soliman FSG. Identification of new 5-(2,6-dichlorophenyl)-3-oxo-2,3-dihydro-5H-thiazolo[3,2-a]pyrimidine-7-carboxylic acids as p38α MAPK inhibitors: design, synthesis, antitumor evaluation, molecular docking and in silico studies. *Bioorg Chem*. 2024;145:107226.
38. Wróbel A, Baradyn M, Ratkiewicz A, Drozdowska D. Synthesis, biological activity, and molecular dynamics study of novel series of a trimethoprim analogs as multi-targeted compounds: dihydrofolate reductase (DHFR) inhibitors and DNA-binding agents. *Int J Mol Sci*. 2021;22(7):3685–3705.
39. Drozdowska D, Wróbel-Tałałaj A, Parzych C, Ratkiewicz A. Benzamide trimethoprim derivatives as human dihydrofolate reductase inhibitors—molecular modeling and in vitro activity study. *Biomedicines*. 2024;12(5):1079–1095.
40. Bondock S, Khalifa W, Fadda AA. Synthesis and antimicrobial evaluation of some new thiazole, thiazolidinone and thiazoline derivatives starting from 1-chloro-3,4-dihydronaphthalene-2-carboxaldehyde. *Eur J Med Chem*. 2007;42(7):948–954.
41. Farghaly TA, Abo Alnaja AM, El-Ghamry HA, Shaaban MR. Synthesis and DNA binding of novel bioactive thiazole derivatives pendent to N-phenylmorpholine moiety. *Bioorg Chem*. 2020;102:104103.
42. Vardevanyan PO, Antonyan AP, Parsadanyan MA, Davtyan HG, Karapetyan AT. The binding of ethidium bromide with DNA: interaction with single- and double-stranded structures. *Exp Mol Med*. 2003;35(6):527–533.
43. Drozdowska D, Bruzgo I, Midura-Nowaczek K. Carbocyclic potential DNA minor groove binders and their biological evaluation. *J Enzyme Inhib Med Chem*. 2010;25(5):629–634.
44. Bruice TC, Mei HY, He GX, Lopez V. Rational design of substituted tripyrrole peptides that complex with DNA by both selective minor-groove binding and electrostatic interaction with the phosphate backbone. *Proc Natl Acad Sci USA*. 1992;89(5):1700–1704.
45. Chaudhary M, Tyagi K. A review on molecular docking and its application. *IJAR*. 2024;12(03):1141–1153.
46. Francesconi V, Giovannini L, Santucci M, Cichero E, Costi MP, Naesens L, Giordanetto F, Tonelli M. Synthesis, biological evaluation and molecular modeling of novel azaspiro dihydrotriazines as influenza virus inhibitors targeting the host factor dihydrofolate reductase (DHFR). *Eur J Med Chem*. 2018;155:229–243.
47. Yang V, Gouveia MJ, Santos J, Kokscha B, Amorim I, Gärtner F, Vale N. Breast cancer: insights in disease and influence of drug methotrexate. *RSC Med Chem*. 2020;11(6):646–664.
48. Brown JI, Persaud R, Iliev P, Karmacharya U, Attarha S, Sahile H, Olsen JE, Hanke D, Idowu T, Frank DA, et al. Investigating the anti-cancer potential of pyrimethamine analogues through a modern chemical biology lens. *Eur J Med Chem*. 2024;264:115971.
49. Ghasemi M, Turnbull T, Sebastian S, Kempson I. The MTT assay: utility, limitations, pitfalls, and interpretation in bulk and single-cell analysis. *Int J Mol Sci*. 2021;22(23):12827–12856.
50. Chaturvedi PR, Decker CJ, Odinecs A. Prediction of pharmacokinetic properties using experimental approaches during early drug discovery. *Curr Opin Chem Biol*. 2001;5(4):452–463.
51. Ekins S, Mestres J, Testa B. In silico pharmacology for drug discovery: methods for virtual ligand screening and profiling. *Br J Pharmacol*. 2007;152(1):9–20.
52. Prasanna S, Doerksen R. Topological polar surface area: a useful descriptor in 2D-QSAR. *Curr Med Chem*. 2009;16(1):21–41.
53. Johnson TW, Dress KR, Edwards M. Using the Golden Triangle to optimize clearance and oral absorption. *Bioorg Med Chem Lett*. 2009;19(19):5560–5564.
54. Callaghan R, Luk F, Bebawy M. Inhibition of the multidrug resistance p-glycoprotein: time for a change of strategy? *Drug Metab Dispos*. 2014;42(4):623–631.
55. Bibi Z. Role of cytochrome P450 in drug interactions. *Nutr Metab (Lond)*. 2008;5(1):1–10.
56. Drozdowska D, Rusak M, Mityk W, Markowska A, Samczuki P. Antiproliferative effects on breast cancer cells and some inter-

- actions of new distamycin analogues with DNA, endonucleases and DNA topoisomerases. *Acta Pol Pharm.* 2016;73(1):47–53.
57. Sigma Aldrich. Technical Bulletin. [accessed 2024 Apr 05]. Available from: <https://www.sigmaaldrich.com/content/dam/sigmaaldrich/docs/Sigma/Bulletin/cs0340bul.pdf>.
 58. Singh UC, Kollman PA. An approach to computing electrostatic charges for molecules. *J Comput Chem.* 1984;5(2):129–145.
 59. Eberhardt J, Santos-Martins D, Tillack AF, Forli S. AutoDock vina 1.2.0: new docking methods, expanded force field, and python bindings. *J Chem Inf Model.* 2021;61(8):3891–3898.
 60. Trott O, Olson AJ. AutoDock Vina: improving the speed and accuracy of docking with a new scoring function, efficient optimization, and multithreading. *J Comput Chem.* 2010;31(2):455–461.
 61. Agarwal R, Smith JC. Speed vs accuracy: effect on ligand pose accuracy of varying box size and exhaustiveness in AutoDock vina. *Mol Inform.* 2023;42(2):2200188.
 62. BIOVIA. Dassault systèmes. Discovery studio visualizer. v21.1.0.20298. San Diego (CA): Dassault Systèmes; 2021.
 63. The PyMOL molecular graphics system, version 1.8. New York (NY): Schrödinger, Inc.; 2015.
 64. Phillips JC, Braun R, Wang W, Gumbart J, Tajkhorshid E, Villa E, Chipot C, Skeel RD, Kalé L, Schulten K, et al. Scalable molecular dynamics with NAMD. *J Comput Chem.* 2005;26(16):1781–1802.
 65. Humphrey W, Dalke A, Schulten K. VMD: visual molecular dynamics. *J Mol Graph.* 1996;14(1):33–38.
 66. Vanommeslaeghe K, MacKerell ADJ. Automation of the CHARMM general force field (CGenFF) I: bond perception and atom typing. *J Chem Inf Model.* 2012;52(12):3144–3154.
 67. Vangipuram M, Ting D, Kim S, Diaz R, Schüle B. Skin punch biopsy explant culture for derivation of primary human fibroblasts. *J Vis Exp.* 2013;77(77):e3779.
 68. Saleh EM, Mohamed FS, Mehanna RA, Essawy MM, Soliman IS. Biocompatibility profile of aged pigmented and non-pigmented silicone elastomer for combined maxillofacial defects. *J Prosthodont.* 2024:1–10.